



In situ observation of photoelectrochemical water oxidation intermediates for selective biomass upgrading with simultaneous hydrogen production

Sandip K. Pahari^{a,b,c}, Yit-Tsong Chen^{a,b,c,*}

^a Department of Chemistry, National Taiwan University, Taipei 10617, Taiwan

^b Institute of Atomic and Molecular Sciences, Academia Sinica, Taipei 10617, Taiwan

^c Department of Electrophysics, PSMC-NYCU Research Center, and LIGHTMED Laser System Research Center, National Yang Ming Chiao Tung University, Hsinchu 300093, Taiwan

ARTICLE INFO

Keywords:

Biomass upgrading
Hydrogen evolution reaction
In situ Raman spectra
Oxygen evolution reaction
Water oxidation intermediates

ABSTRACT

In a water-splitting reaction, the anodic biomass upgrading with the simultaneous cathodic hydrogen production is a promising sustainable energy development for future needs. In the electrocatalytic water oxidation process, the reactive intermediates generated in the oxygen evolution reaction (OER) can be used for the selective oxidation of organic molecules to value-added chemicals. Herein, we fabricated a multifunctional catalyst, composed of phosphate-functionalized few-layer phosphorene (FLP-P) and bismuth ferrite (BFO) nanosheets (referred to as FLP-P-BFO), for photoelectrochemical (PEC) water-splitting reactions with the advantages of an efficient charge separation and the hybrid excitations of electrons and photons. At the cathode, the PEC-assisted FLP-P-BFO-catalytic reaction exhibits excellent hydrogen evolution reaction (HER) activity of a low overpotential of 110 mV at 10 mA cm⁻² and a small Tafel slope of 51 mV dec⁻¹. At the anode, the high FLP-P-BFO-catalytic efficiency is attributed to the bifunctional mechanism, in which the functionalized phosphate groups help to stabilize the Fe-OOH intermediate, thus mitigating the energy demand in the OER process. The bifunctional mechanism was validated by both pH-dependent and isotope-labeling examinations. With the assistance of *in situ* Raman spectroscopy, the optimal electrochemical conditions for the maximal production of the Fe-OOH intermediate in OER were obtained for the biomass upgrading of 5-hydroxymethylfurfural (HMF) to 2,5-furandicarboxylic acid (FDCA) with 100% conversion and selectivity, but without reducing the HER activity. The anodic biomass conversion, from HMF (a carbon-neutral feedstock) to the high value-added FDCA (a monomer of bio-plastics), with the simultaneous cathodic H₂ production is a promising sustainable energy innovation. This novel strategy of employing PEC-assisted FLP-P-BFO-catalytic biomass upgrading to value-added products is extendable to combine the cathodic HER with many other anodic hydrocarbon oxidations for future energy-related applications.

1. Introduction

The renewable energy-driven hydrogen production from photoelectrochemical (PEC) water splitting has been widely recognized as a promising sustainable energy approach for future needs [1,2]. Despite the fact that the realization of large-scale water splitting is hindered mainly by the slow kinetics of the anodic half reaction (i.e., oxygen evolution reaction, OER), O₂ as the end product of OER is ironically not of high economical value [3,4]. In addition, during the water electrolysis, H₂ and O₂ are produced simultaneously, which might lead to the formation of an explosive H₂/O₂ mixture [5]. The OER also imposes performance limit on the water-splitting process due to difficulties of

forming the catalyst-bound reactive oxygen species (ROS, such as the M-OH, M=O, and M-OOH intermediates with M representing a reactive metal-catalyst center). Among these intermediates, the formation of M-OOH via the nucleophilic attack of a water molecule on M=O is regarded as an energetically demanding step [6]. Nevertheless, the ROS generated on the catalyst can be used to selectively oxidize various substrates to target chemicals. An alternative strategy to gain high value-added products, via the ROS-catalyzed reactions in water splitting, is to replace the challenging, but less valuable, OER with economically more attractive organic oxidative reactions [7]. Such a novel approach will not only lower the electrochemical voltage input to exclude the explosive H₂/O₂ gas-mixture, but also produce more

* Corresponding author.

E-mail address: yt22@nycu.edu.tw (Y.-T. Chen).

<https://doi.org/10.1016/j.cej.2023.145232>

Received 12 May 2023; Received in revised form 8 July 2023; Accepted 3 August 2023

Available online 5 August 2023

1385-8947/© 2023 Elsevier B.V. All rights reserved.

consequently, the employed electrocatalysts could suffer from unsatisfying catalytic performance [22].

In the FLP-P-BFO-assisted OER of this study, the Fe centers of BFO offer the iron-oxo intermediate formation (e.g., Fe-OOH) and the phosphate groups modified on FLP help to stabilize the Fe-OOH complex via a proton transfer. With the assistance of *in situ* Raman spectroscopy, we were able to identify the key intermediates (Fe=O and Fe-OOH) during the OER process and determine the reaction mechanism based on experimental observations. Taking advantage of the *in situ* Raman identification, we optimized the electrochemical potential for the maximal production of Fe-OOH to catalyze the HMF oxidation, and obtained a complete biomass upgrading from HMF to FDCA (with 100% conversion and selectivity). This approach to achieve an efficient anodic biomass conversion to value-added chemicals with the simultaneous cathodic H₂ production can be extended to many other oxidative biomass valorization for diverse energy-related applications.

2. Results and discussion

Shown in Fig. 1 are the bright-field transmission electron microscopy (TEM) images of thin-layered FLP-P (Fig. 1b), FLP (Fig. S1a of the Supporting Information), and BFO (Fig. 1c). The high-resolution transmission electron microscopy (HR-TEM) images further reveal the periodic lattice fringes of 0.26 nm for the (012) planes of black phosphorus (in the inset of Fig. 1b) and 0.23 nm for the (002) planes of BFO (in the inset of Fig. 1c) [23]. The TEM and HR-TEM images of FLP-P-BFO (Fig. 1d, and Fig. S1b) show the stacking layers of BFO and FLP-P to form a heterostructure. Fig. 1e presents the Raman scattering spectra of the FLP-P-BFO hybrid and its constituents; while BFO contains two characteristic modes of A₁-1 and A₁-2 at 128.2 and 172.5 cm⁻¹,

respectively, FLP-P possesses the out-of-plane (A_g¹) and in-plane (B_{2g} and A_g²) vibrational modes at 370.7, 448.2, and 476.5 cm⁻¹ [24]. The Raman signals of BFO and phosphorene confirm the presence of both constituents in the FLP-P-BFO hybrid.

The chemical states of the elements in the as-prepared FLP-P-BFO compositions were analyzed by X-ray photoelectron spectroscopy (XPS) with the survey spectrum showing the Bi, Fe, P, and O elements present in FLP-P-BFO (Fig. S2). In the Bi 4f core-level spectrum (Fig. S3a), the strong doublet signals at 156.4 and 161.7 eV correspond to Bi 4f_{7/2} and Bi 4f_{5/2}, respectively. There is no trace of the metallic Bi⁰, Bi²⁺, and Bi⁵⁺ 4f core levels, indicating that only the Bi³⁺ state is present in FLP-P-BFO. In the Fe 2p XPS spectrum of FLP-P-BFO (Fig. S3b), the signals at 708.2 and 721.6 eV are assigned respectively to the Fe 2p_{3/2} and Fe 2p_{1/2} doublets of Fe³⁺, due to the spin-orbit interaction. The satellite peaks in the Fe 2p spectrum are also in good agreement with those of Fe³⁺ in BFO reported previously [23]. The existence of phosphorus in FLP-P-BFO is supported by the P 2p core-level XPS spectrum (Fig. 1f), including the spin-orbit doublets of P 2p_{3/2} and P 2p_{1/2} at 129.1 and 130.0 eV, respectively, and the broad PO_x signal at ~134.0 eV [24]. In addition, the iron-oxygen bond (Fe-O), the surface dangling bond (O·), and the adsorbed oxygen (O₂ and/or H₂O) of FLP-P-BFO are responsible for the O 1s core-level peaks at 527.1, 528.6, and 529.8 eV, respectively (Fig. S3c) [25]. The phosphate groups modified on FLP-P-BFO are further confirmed by the stretching vibrations of the P-O (at 1012 cm⁻¹) and P=O (at 1389 and 1641 cm⁻¹) bonds observed in Fourier-transform infrared (FTIR) spectrum (Fig. 1g) [26].

To compare the kinetics of photo-generated charge carriers at the electrode-electrolyte interface in the PEC-catalytic OER using 0.5 M Na₂SO₄ solution as an electrolyte and different electrodes (FLP-P, BFO, and FLP-P-BFO), electrochemical performances were investigated either

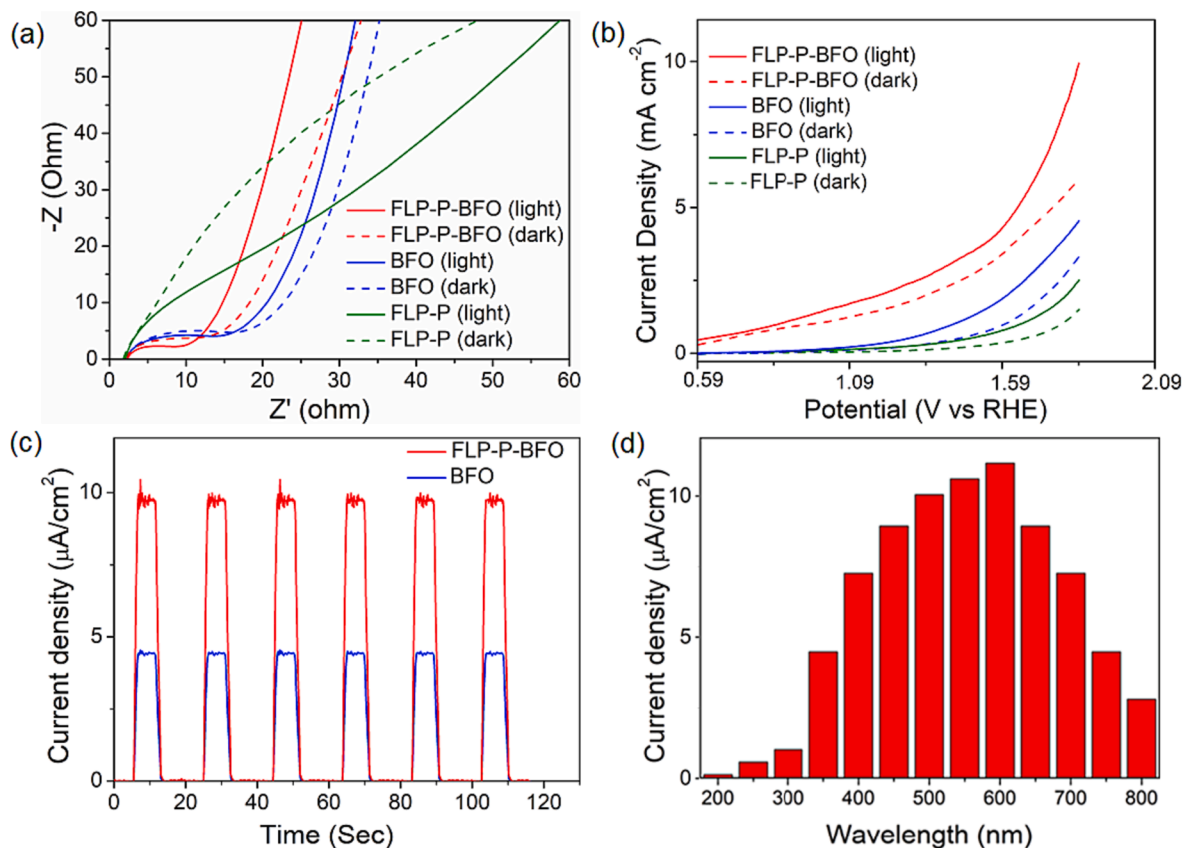


Fig. 2. (a–b) The PEC-catalytic characteristics of the FLP-P, BFO, and FLP-P-BFO photoelectrodes were tested by measuring their (a) Nyquist plots and (b) LSV profiles scanned at 10 mV s⁻¹ under visible-light illumination and in the dark conditions. (c) The transient photocurrents of FLP-P-BFO and BFO were measured to compare their photoswitchings in response to a train of pulsed visible-light illumination. (d) The wavelength-dependent photocurrent density of the FLP-P-BFO photoelectrode was measured at 200–800 nm.

in the dark, or under visible-light illumination (generated by an LED-based solar simulator with the light intensity of 50 mW cm^{-2}). Hereafter, $0.5 \text{ M Na}_2\text{SO}_4$ solution as an electrolyte and the visible-light illumination of 50 mW cm^{-2} were applied to the PEC-catalytic experiments throughout this study, unless otherwise stated. Shown in Fig. 2a are the Nyquist plots acquired by electrochemical impedance spectroscopy (EIS), among which the semicircular arc (R_{ct}) of FLP-P-BFO is smaller than those of FLP-P and BFO (in the case either with, or without, illumination). Since the R_{ct} of EIS represents an electron-transfer resistance, the smaller arc diameter indicates the lower electron-transfer resistance at the electrode–electrolyte interface and accordingly the easier transportation of electron-hole pairs. Moreover in Fig. 2a, the R_{ct} value measured with FLP-P-BFO under visible-light illumination (the red solid line) is smaller than that in the dark (the red dashed line), revealing the effective separation of photo-excited electron-hole pairs and the fast interfacial charge transfer on the FLP-P-BFO surface under visible-light excitation. Similarly, the smaller R_{ct} values of FLP-P and BFO were observed with visible-light excitation (cf. in the dark), although their R_{ct} values are not as small as that of FLP-P-BFO. In Fig. S5, the positive slopes in the Mott-Schottky measurements for BFO and FLP-P-BFO indicate that both possess n-type conductivity. The flat band potentials (V_{FB}) were estimated to be -0.08 V (vs. RHE) for BFO and -0.16 V (vs. RHE) for FLP-P-BFO. The more negative V_{FB} value of FLP-P-BFO, than that of BFO, reveals the more effective increase of the charge carrier concentration and higher photoelectrocatalytic activity in FLP-P-BFO [27].

To investigate the surface reactivity of the FLP-P-BFO photoelectrode, linear sweep voltammetry (LSV) was performed with, or without, visible-light illumination. As displayed in Fig. 2b, the current density is much higher by using FLP-P-BFO than FLP-P and BFO,

irrespective of visible-light illumination, which can be attributed to more active sites existing on the FLP-P-BFO surface. It is also noted that by using FLP-P-BFO, a noticeable improvement in the current density was obtained with visible-light excitation (cf. in the dark). In Fig. 2c, the photoswitching of FLP-P-BFO was examined by measuring its transient photocurrent response, where the photocurrent increases drastically upon visible-light illumination and reverts to its initial state after turning off the light. Notably, FLP-P-BFO responds with much higher photocurrent density than BFO, signifying the superior PEC capabilities of FLP-P-BFO in reversibility, photostability, and efficiency. These outcomes demonstrate that FLP-P-BFO can be utilized as a highly efficient visible-light-driven photocatalyst. In Fig. 2d, the excellent visible-light response of FLP-P-BFO is shown with the wavelength-dependent photocurrent measurement at $200\text{--}800 \text{ nm}$, revealing that the highest current density can be achieved by $\sim 600\text{-nm}$ light excitation.

The catalytic HER performance of the as-prepared photoelectrodes in a three-electrode system was tested with visible-light excitation. Fig. 3a shows the polarization curves in the PEC-catalytic HER using various electrodes of FLP-P-BFO, FLP-P, BFO, and 20 wt\% Pt/C . The overpotential of 110 mV at a current density of 10 mA cm^{-2} was measured for FLP-P-BFO, which is close to 90 mV of Pt/C and significantly lower than 240 and 310 mV of FLP-P and BFO, respectively. In Fig. 3b, the Tafel slope of 51 mV dec^{-1} was determined for FLP-P-BFO, which is smaller than those of FLP-P (64 mV dec^{-1}) and BFO (68 mV dec^{-1}), demonstrating the faster reaction kinetics in FLP-P-BFO with its HER route following the Volmer-Heyrovsky mechanism [28]. Moreover, the HER performance of FLP-P-BFO is superior to most of the reported Fe- or P-based electrodes (as listed in Table S1). In Fig. 3c, the chronoamperometric response measured with the FLP-P-BFO photoelectrode in HER displays a very little attenuation within 24 h , presenting its

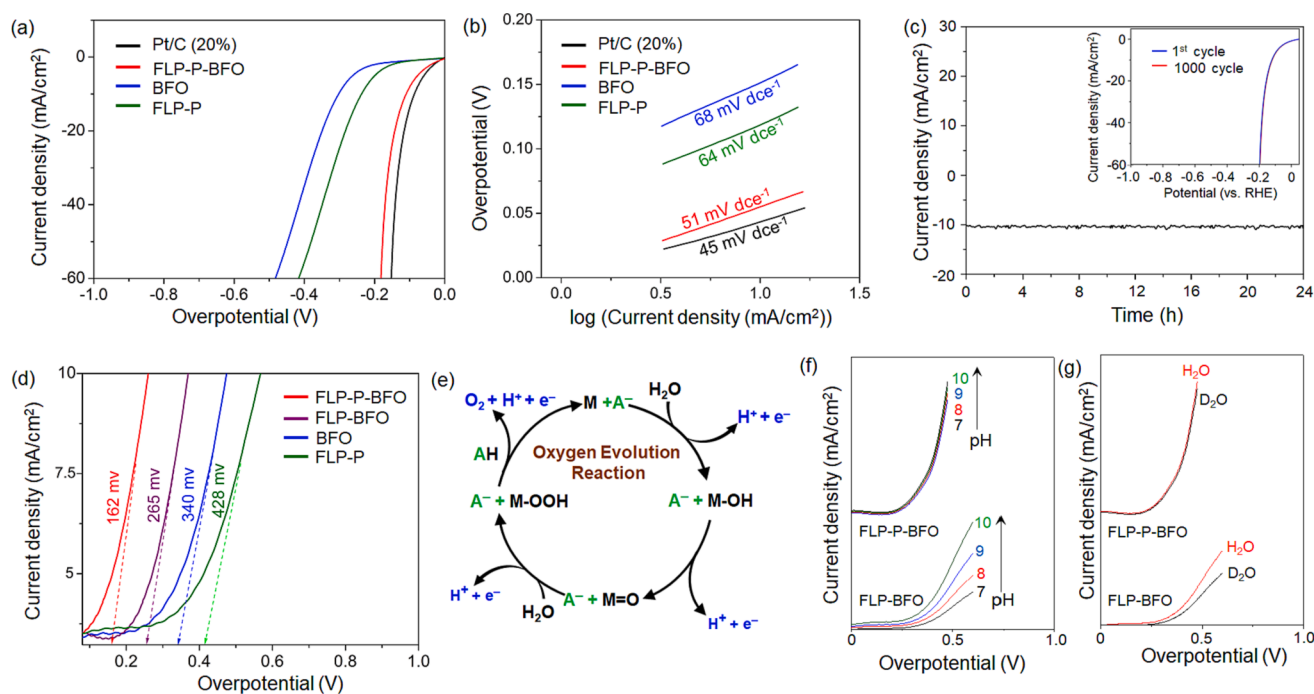


Fig. 3. A comparison for the PEC-catalytic performance in (a–c) cathodic HER and (d–g) anodic OER with different photoelectrodes under visible-light illumination. (a) The polarization curves of HER were scanned at 10 mV s^{-1} . (b) The Tafel plots were derived from the HER polarization curves of (a). (c) The cycling stability of an FLP-P-BFO photoelectrode used in HER was tested. (inset) The polarization curves were measured before and after the stability test. (d) The polarization curves of OER using different photoelectrodes were scanned at 20 mV s^{-1} with their overpotentials labelled. (e) The bifunctional mechanism in OER involves two catalytic active centers, a reactive metal center (M) and a proton acceptor (A^-), to work cooperatively. In the FLP-P-BFO-catalytic reaction, the two catalytic active centers are the Fe atoms of the BFO moiety acting as the reactive metal center ($M=\text{Fe}$) and the phosphate groups functionalized on the FLP-P moiety serving as the proton acceptor ($A^- = \text{PO}_4^-$). During the nucleophilic attack of H_2O on $\text{Fe}=\text{O}$, the catalytic center (Fe) provides an active site to form the metal-oxo intermediate ($\text{Fe}-\text{OOH}$), while the proton acceptor (PO_4^-) helps to stabilize the hydroperoxyl side of $\text{Fe}-\text{OOH}$. (f–g) The OER activity and proton-diffusion kinetics at the electrolyte/catalyst interface of the FLP-BFO or FLP-P-BFO photoelectrode were investigated with the LSV measurements (f) at different pH environments from 7 to 10 and (g) with $0.5 \text{ M Na}_2\text{SO}_4$ dissolved in H_2O , compared to D_2O , as an electrolyte.

excellent electrode stability. Also, the polarization curve (shown in the inset of Fig. 3c) exhibits a negligible change after running 1000 cycles in the potential range from 0 to -1 V.

In Fig. 3d, the photocatalytic efficiencies of FLP-P, BFO, FLP-BFO, and FLP-P-BFO in OER were further tested by LSV, giving the overpotentials (η) of 0.428, 0.340, 0.265, and 0.162 V, respectively. In particular, the η value of FLP-P-BFO is lower than that of FLP-BFO, manifesting that the functionalized phosphate groups improve the electrocatalytic reactivity of the FLP-P-BFO photoelectrode. In addition to the enhancement of electrocatalytic reactivity, we further examined the role of the functionalized phosphate groups of FLP-P-BFO in the OER process. As depicted in Fig. 3e, the formation of the M–OOH intermediate in OER via the attack of a water molecule to M=O is regarded as an energy-demanding step. Nevertheless, if the proton can be transferred from M–OOH to a neighboring acceptor (A^-), the energy barrier will be reduced significantly [16–18]. It is also known that except the neighboring acceptor ($A^- = PO_4^-$ in this study), the OH^- anion in solution could assist the proton transfer as well. To this end, we analyzed the proton transfers in the FLP-BFO- and FLP-P-BFO-catalytic OER in different pH environments. By varying pH from 7 to 10 (Fig. 3f), the OER efficiency changes notably in the FLP-BFO-catalytic reactions, in sharp contrast to the negligible variation when using FLP-P-BFO as an electrocatalyst. These results demonstrate that the phosphate groups of FLP-P-BFO expedited the de-protonation process. Consequently, changing the pH value has little impact on the FLP-P-BFO-catalytic OER efficiency.

To further validate the proton transfer through the functionalized phosphate groups (of FLP-P-BFO), cf. via an environmental OH^- electrolyte (when using FLP-BFO), we conducted an isotope-labeling test to compare the proton (H/D)-transfer kinetics in H_2O and D_2O . If the proton transfer is assisted with the OH^- in an environmental electrolyte, the proton-transfer kinetics in D_2O , cf. in H_2O , should decelerate significantly by 1.6–5 times [29]. As shown in Fig. 3g, the OER activities of FLP-BFO and FLP-P-BFO in H_2O or D_2O are compared, where the FLP-BFO-catalytic reactions exhibit a strong H/D dependence with a drastic decrease of the OER current in D_2O . In stark contrast, very weak H/D influence was observed in the FLP-P-BFO-catalytic OER, supporting that the interfacial proton transfer was facilitated by the functionalized phosphate groups to substantially improve the electrocatalytic reactivity. In addition, a durability test of FLP-P-BFO in OER shows that the polarization curve exhibits a negligible change after running 1000 cycles (Fig. S6a) and the chronoamperometric response displays a very little attenuation in 24 h (Fig. S6b). The overpotentials measured in OER using our FLP-P-BFO and other literature-reported catalysts are listed in Table S2 for comparison, in which FLP-P-BFO is demonstrated to be one of the best catalysts for OER.

However, the enhancement of the electrocatalytic reactivity of FLP-P-BFO in OER, relative to FLP-BFO, may associate with the increase in surface area and/or electrical conductivity of FLP-P-BFO by phosphate functionalization. To analyze variation of the surface area, we determined the specific activities of the FLP-P-BFO and FLP-BFO electrodes by measuring their Brunauer-Emmett-Teller (BET, Fig. S4) and electrochemical active surface areas (ECSA, Fig. S7). Compared with those presented in Fig. 3d, the LSV curves normalized with BET and ECSA (as shown in Fig. S8) indicate no apparent changes for the OER efficiencies of FLP-BFO and FLP-P-BFO, demonstrating that an increase of surface area by phosphate functionalization is negligible. Next, the effect of the phosphate functionalization on electrical conductivity was investigated by EIS using the FLP-P-BFO and FLP-BFO electrodes (Fig. S9), where no enhancement of the electrical conductivity is found for FLP-P-BFO. Considering the phosphate functionalization has caused negligible changes in both surface area (Fig. S8) and electrical conductivity (Fig. S9), but a significant increase in electrocatalytic reactivity (Fig. 3d), the role of the phosphate groups of FLP-P-BFO to assist the proton transfer in OER is further confirmed as proposed in the bifunctional mechanism (Fig. 3e).

In the FLP-P-BFO-catalytic OER, *in situ* Raman spectroscopy was employed to find the optimal electrochemical conditions of producing the oxygenated intermediates, such as Fe=O, Fe–OOH, etc. However, the detection of reactive chemical intermediates in OER is challenging because of the rapid oxygen evolution. Accordingly, the steady-state concentrations of the reactive intermediates are extremely low, making the spectroscopic detection even more difficult in a liquid environment. Nevertheless, we addressed this problem of probing the OER-intermediates in our recent *in situ* Raman spectroscopic study by using a mixture of acetonitrile:water = 5:1 (represented by AcCN:H₂O (5:1)), rather than pure water, as an electrolyte to slow down the OER kinetics for successful observation of the reactive intermediates [18,20]. In Fig. 4a, using the AcCN:H₂O (5:1) electrolyte in the FLP-P-BFO-catalytic OER, we began to observe a Raman signal at ~ 896 cm^{-1} when the electrochemical potential was increased to 0.83 V. The Raman signal at ~ 896 cm^{-1} is attributed to the vibration of the Fe=O intermediate, of which the spectral intensity grows further at a potential higher than 0.83 V, reaches a maximum at 1.09 V, then decreases, and finally vanishes at 1.39 V. Interestingly, while the Fe=O peak at ~ 896 cm^{-1} decreases, a new signal at ~ 810 cm^{-1} begins to emerge at 1.09 V (Fig. 4a), strongly implicating the formation of another intermediate (e.g., Fe–OOH). To support the existence of Fe–OOH, we searched for the superoxide stretching (denoted by –O–O–) of this intermediate. In Fig. 4b, the peak at ~ 1149 cm^{-1} shows up and disappears simultaneously with the vibrational signal at ~ 810 cm^{-1} (Fig. 4a) in the potential range of 1.09–1.49 V, indicating that both peaks at ~ 1149 and ~ 810 cm^{-1} should originate from the same chemical species. From previous reports, the stretching vibration of superoxides (–O–O–) appears typically in the range of 1000–1200 cm^{-1} [30]. Accordingly, we assigned the Raman signal observed at ~ 1149 cm^{-1} to the –O–O– stretching of the Fe–OOH intermediate. Furthermore, the stretching of Fe=O in many iron complexes has been reported to be around 800–860 cm^{-1} [31,32]. It is also noted that the Fe–O bond of the Fe–OOH intermediate involves some extent of a double-bond characteristic, due to the donation of electron density from the superoxide to the Fe center [33]. Thus, we assigned the Fe–O stretching of Fe–OOH to be responsible for the Raman signal at ~ 810 cm^{-1} .

In addition, we applied an isotope (H/D)-labeling test to further validate the existence of Fe–OOD by substituting the AcCN:D₂O (5:1) mixture as an electrolyte in the above PEC-assisted FLP-P-BFO-catalytic OER. Compared with the vibrational signals of Fe–OOH (observed in Fig. 4a–b), the stretching vibrations of Fe–O and –O–O– in Fe–OOD (observed in Fig. 4c–d) were red-shifted by 10 cm^{-1} (from 810 to 800 cm^{-1}) and 23 cm^{-1} (from 1149 to 1126 cm^{-1}), respectively, where the more prominent red-shift in –O–O–, than in Fe–O, stems obviously from the adjacency of the deuterium (D) to the vibrating site. In the isotope-labeling experiment, because the signal at ~ 896 cm^{-1} does not change its position after deuteration (cf. Fig. 4a and Fig. 4c) and the observed vibrational frequency is close to the Fe=O stretching range [31,32], the above assignment of this peak at ~ 896 cm^{-1} to the stretching mode of the Fe=O intermediate is further justified.

From the spectroscopic investigation of Fig. 4a–b, the maximal production of Fe–OOH in the FLP-P-BFO-catalytic OER was found to occur at the electrochemical potential of 1.39 V. In the following FLP-P-BFO-catalytic biomass upgrading experiments, we fixed the potential at 1.39 V to gain Fe–OOH for oxidizing HMF to FDCA. For the electrocatalytic oxidation of HMF in an aqueous electrolyte, OER is the major competing reaction. In Fig. 5a, the LSV profiles with the BFO, FLP-P, and FLP-P-BFO photoelectrodes were scanned, in the presence or absence of 5 mM HMF, to compare their PEC-catalytic performances. With the FLP-P photoelectrode, when O₂ bubbles began to be generated on the working electrode, the onset potential (E_{onset}) of the water oxidation reaction was measured to be 1.65 V. After adding HMF, the E_{onset} shifted very slightly to a lower potential, together with a tiny increase in the current density. These results suggest that FLP-P possesses no selectivity toward the HMF oxidation. For the BFO photoelectrode, the E_{onset} of

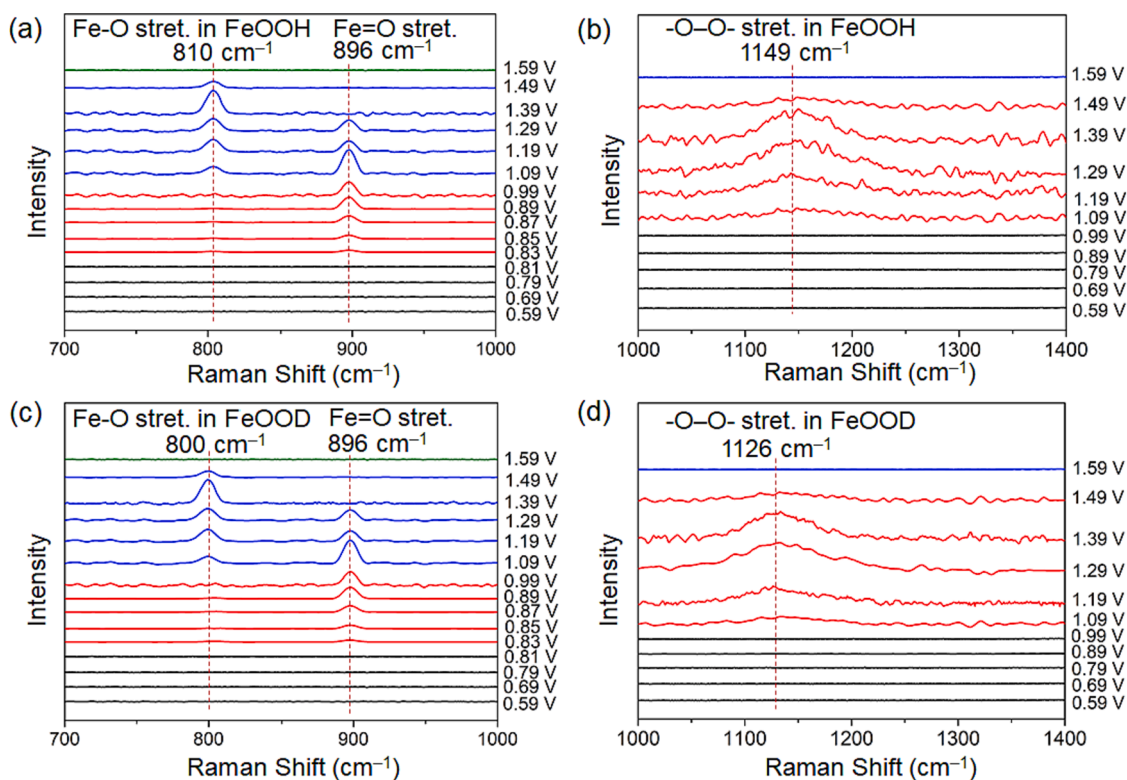


Fig. 4. (a–b) In the PEC-assisted FLP-P-BFO-catalytic OER with 0.5 M Na_2SO_4 dissolved in $\text{AcCN}:\text{H}_2\text{O}$ (5:1) as an electrolyte, the 488-nm laser-excited *in situ* Raman spectra were scanned at 700–1400 cm^{-1} with a stepwise increase in the electrochemical potential. While the stretching vibration of the $\text{Fe}=\text{O}$ intermediate is responsible for the signal at $\sim 896 \text{ cm}^{-1}$, the peaks at ~ 810 and $\sim 1149 \text{ cm}^{-1}$ are due to the $\text{Fe}-\text{O}$ and $-\text{O}-\text{O}-$ stretchings of the $\text{Fe}-\text{OOH}$ intermediate, respectively. (c–d) The Raman spectra were scanned with the same experimental conditions as those of (a–b), except that 0.5 M Na_2SO_4 was dissolved in $\text{AcCN}:\text{D}_2\text{O}$ (5:1). The stretching vibrations of $\text{Fe}=\text{O}$ and the $\text{Fe}-\text{O}$ and $-\text{O}-\text{O}-$ of the $\text{Fe}-\text{OOD}$ intermediate are responsible for the observed signals at ~ 896 , ~ 800 , and $\sim 1126 \text{ cm}^{-1}$, respectively.

1.52 V (for the water oxidation) and a significantly higher current density (than that of FLP-P) were observed, revealing that BFO is more electrochemically active than FLP-P. After introducing HMF, while E_{onset} reduced from 1.52 V to ~ 1.1 V (for the HMF oxidation), the E_{onset} of generating O_2 bubbles was measured ~ 1.52 V (for the water oxidation). These outcomes indicate that BFO was reactive for both HMF and water oxidations. In contrast, when using FLP-P-BFO, the E_{onset} of ~ 1.1 V was obtained after adding HMF; meanwhile, no bubbles were detected. This result demonstrates that the HMF oxidation was a preferable reaction to the FLP-P-BFO-supported $\text{Fe}-\text{OOH}$ intermediate, which is similar to previous reports [34,35]. In Fig. 5b, the kinetics of converting HMF to FDCA with different photoelectrodes were tested. After an 80-min reaction, the FLP-P-BFO-catalytic oxidation of HMF to FDCA could reach 100% conversion and selectivity, in comparison with the FLP-P and BFO electrodes of the less conversion rates of 5% and 82%, respectively.

To determine the electrical and illuminant contributions in the PEC-assisted FLP-P-BFO-catalytic oxidation of HMF to FDCA, we applied various catalytic methods for the test, including electrocatalysis, photocatalysis, and PEC-catalysis. In Fig. S11, the efficiency of the FLP-P-BFO-catalytic HMF conversion reveals that the hybrid excitations of electrons and photons can substantially enhance the HMF conversion, of which the result also supports the general advantage of a PEC-catalytic reaction (with the interplay between electro- and photo-enhancements). Moreover, in the FLP-P-BFO-catalytic biomass upgrading reaction, the efficiency of generating photo-induced electron-hole pairs in the initial step and forming the anodic iron-oxo intermediates during the oxidation process (as illustrated in Fig. 3e) should be vital to the whole biomass conversion. To discern the roles of electrons, holes, and the iron-oxo intermediates ($\text{Fe}-\text{OH}$ and $\text{Fe}-\text{OOH}$) in the PEC-assisted FLP-P-BFO-catalytic HMF oxidation to FDCA, we applied specific radical-scavengers in

this biomass conversion reaction. The active species selected for the radical-scavenger experiment include $\text{K}_2\text{S}_2\text{O}_8$ (an electron scavenger), Na_2SO_3 (a hole scavenger), 1,4-benzoquinone (BQ, an $\cdot\text{O}_2^-$ scavenger), and *tert*-butanol (t-BuOH, a $\cdot\text{OH}$ scavenger). The experimental results shown in Fig. 5c clearly indicate that the HMF conversion efficiency decreases significantly after introducing Na_2SO_3 (a hole scavenger) or BQ (an $\cdot\text{O}_2^-$ scavenger), manifesting that both holes and the hole-promoted $\text{Fe}-\text{OOH}$ intermediate are predominant in the HMF oxidation. From this HMF conversion experiment, we also note that the FLP-P-BFO electrode is of excellent electrocatalytic durability without a significant loss of efficiency after eight reaction cycles (Fig. S12 and Fig. S13).

As illustrated in Fig. S14, two reaction pathways are possibly involved in the HMF oxidation. One is to form the DFF intermediate via an initial alcohol oxidation, and the other is to generate the HMFC intermediate through an aldehyde oxidation. Nevertheless, both pathways converge toward the formation of FFCA prior to FDCA. From a gas chromatography (GC)-mass spectrometry (MS) analysis of the reaction intermediates (Fig. S10), we confirmed that the pathway is via DFF to form FFCA, and finally to produce FDCA, which is similar to the other reported oxidation reactions in neutral medium [36]. Based on these experimental results, a proposed reaction mechanism for converting HMF to FDCA is illustrated in Fig. 5d.

Finally, given the excellent photoelectrocatalytic performance of FLP-P-BFO in the HMF oxidation with the simultaneous HER, we assembled a two-electrode electrolyzer (Fig. S15), using the same experimental conditions as the three-electrode system used in this work (see Methods), to test whether the anodic HMF conversion was impeded by the cathodic H_2 production [37,38]. With this two-electrode configuration, a long-term electrolysis with a constant cell voltage of 1.39 V

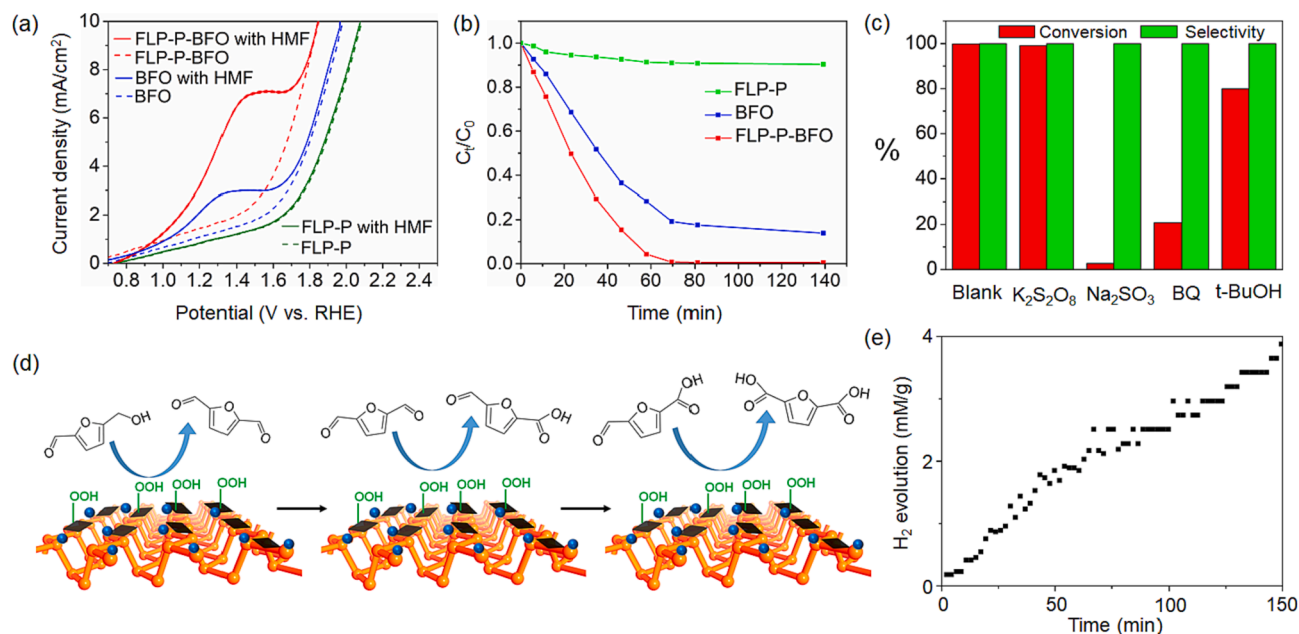


Fig. 5. The PEC-catalytic oxidation of HMF to FDCA with different photoelectrodes under visible-light illumination was investigated. (a) The LSV profiles were scanned with different photoelectrodes for the biomass upgrading, in the presence or absence of 5 mM HMF. (b) The kinetics of converting HMF to FDCA with different photoelectrodes is presented by the normalized time-dependent concentration (C_t/C_0) of HMF. After the conversion reaction, the FDCA product was analyzed by high-performance liquid chromatography (HPLC). (c) The conversion and selectivity rates of the HMF oxidation to FDCA were measured in a one-hour FLP-P-BFO-catalytic OER accompanied with various free-radical scavengers (5 mM), including $K_2S_2O_8$ (an electron scavenger), Na_2SO_3 (a hole scavenger), 1,4-benzoquinone (BQ, an $\cdot O_2^-$ scavenger), and *tert*-butanol (t-BuOH, a $\cdot OH$ scavenger). The Blank columns represent no scavengers involved in the reaction. In the PEC-catalytic conversion of 10 mM HMF to FDCA with an FLP-P-BFO photoelectrode, (d) the oxidation route of HMF to FDCA at the surface of FLP-P-BFO assisted with the Fe-OOH intermediate and (e) the HER conversion rate are examined. In (e), the quantity of the generated H_2 gas was measured by GC-MS.

was applied to generate H_2 , which was quantified subsequently by GC-MS (as shown in Fig. 5e). In parallel with the stable cathodic HER, the efficiency of the simultaneous anodic HMF conversion was not interfered with the H_2 production as demonstrated by the unaltered polarization curves shown in Fig. S16. The performance of FLP-P-BFO is also superior to those of the reported electrocatalysts for the oxidation of HMF to FDCA (Table S3).

3. Conclusion

We have demonstrated a facile, efficient PEC-assisted FLP-P-BFO-catalytic water-splitting reaction in neutral medium for anodic biomass upgrading with the simultaneous cathodic H_2 production. At the cathode, the PEC-assisted FLP-P-BFO-catalytic reaction exhibits the excellent HER activity of a low overpotential of 110 mV at 10 mA cm^{-2} and a small Tafel slope of 51 mV dec^{-1} . At the anode, the excellent photoelectrocatalytic reactivity of FLP-P-BFO was resulted from the hybrid excitation of electrons and photons, the efficient charge separation, and the functionalized phosphate groups of FLP-P-BFO to stabilize the Fe-OOH intermediate via a bifunctional mechanism. The bifunctional mechanism was validated by both pH-dependent and isotope-labelling tests. *In situ* Raman spectroscopy was employed to detect the transient intermediates in the FLP-P-BFO-catalytic OER using the AcCN:H₂O (5:1) mixture as an electrolyte, which determined the optimal electrochemical conditions of forming the Fe-OOH intermediate in OER for the biomass upgrading of HMF to FDCA. The anodic biomass conversion, from HMF to the high value-added FDCA of 100% conversion and selectivity, with the simultaneous cathodic H_2 production is a promising sustainable energy development for future needs. This novel strategy of employing PEC-assisted FLP-P-BFO-catalytic biomass upgrading to value-added products is extendable to combine the cathodic HER with many other anodic hydrocarbon oxidations for future energy-related applications.

4. Experimental section

The detailed experimental methods and procedures are all provided in the Supporting Information, including experimental methods (Section A), structural determination and surface area analysis (Section B), photoelectrochemical measurements (Section C), biomass conversion (Section D), comparison of the HER performance for different catalysts (Table S1), comparison of the OER performance for different catalysts (Table S2), and electrocatalytic performances of the recently reported electrocatalysts for the HMF oxidation to FDCA (Table S3). Only a short and brief description is given in this section.

5. Preparation of photoelectrocatalysts

0.5 M HNO_3 solution containing $Bi(NO_3)_3 \cdot 5H_2O$, $Fe(NO_3)_3 \cdot 9H_2O$, and 2 M citric acid was dried and further calcined to produce BFO. FLP was prepared from the liquid-phase exfoliation of bulk black phosphorus using N-methyl-2-pyrrolidone (NMP) as a solvent under Ar atmosphere. FLP-P was produced by the air oxidation of FLP at 50 °C. FLP-P-BFO was produced first by liquid-phase exfoliation of a solution containing black phosphorus and BFO to form FLP-BFO, which was then oxidized in the air to FLP-P-BFO at 50 °C.

6. Photoelectrochemical measurements

Using an Autolab potentiostat, all electrochemical measurements were performed with 0.5 M Na_2SO_4 as an electrolyte solution, an Ag/AgCl electrode and a Pt wire serving as the reference and counter electrodes, respectively. In all PEC experiments, a 200-W LED-based solar simulator was used as the illumination source.

7. Biomass conversion

The HMF oxidation reactions were conducted in 0.5 M Na_2SO_4

solution. For the two-electrode electrolysis, FLP-P-BFO was employed as the catalyst for both anode and cathode. The identification and quantification of the products were determined by GC-MS and HPLC.

Declaration of Competing Interest

The authors declare that they have no known competing financial interests or personal relationships that could have appeared to influence the work reported in this paper.

Data availability

Data will be made available on request.

Acknowledgments

This work was supported, in part, by the Ministry of Science and Technology (MOST) of Taiwan under Grant nos. 110-2113-M-002-017, 111-2113-M-A49-037-MY2, and 111-2811-M-A49-552.

Appendix A. Supplementary data

Supplementary data to this article can be found online at <https://doi.org/10.1016/j.cej.2023.145232>.

References

- P.V. Kamat, K. Sivula, Photoelectrochemical and photocatalytic hydrogen generation: A virtual issue, *ACS Energy Lett.* 7 (12) (2022) 4379–4380.
- K. Sivula, R. van de Krol, Semiconducting materials for photoelectrochemical energy conversion, *Nat. Rev. Mater.* 1 (2016) 185–196.
- H. Ding, H. Liu, W. Chu, C. Wu, Y.i. Xie, Structural transformation of heterogeneous materials for electrocatalytic oxygen evolution reaction, *Chem. Rev.* 121 (21) (2021) 13174–13212.
- E. Fabbri, T.J. Schmidt, Oxygen evolution reaction-The enigma in water electrolysis, *ACS Catal.* 8 (10) (2018) 9765–9774.
- P.J. McHugh, A.D. Stergiou, M.D. Symes, Decoupled electrochemical water splitting: from fundamentals to applications, *Adv. Energy Mater.* 10 (2020) 2002453.
- J. Zhang, H.B. Tao, M. Kuang, H.B. Yang, W. Cai, Q. Yan, Q. Mao, B. Liu, Advances in thermodynamic-kinetic model for analyzing the oxygen evolution reaction, *ACS Catal.* 15 (2020) 8597–8610.
- X.M.C. Ta, R. Daiyan, T.K.A. Nguyen, R. Amal, T. Tran-Phu, A. Tricoli, Alternatives to water photooxidation for photoelectrochemical solar energy conversion and green H₂ production, *Adv. Energy Mater.* 12 (2022) 2201358.
- S. Kar, D. Milstein, Oxidation of organic compounds using water as the oxidant with H₂ liberation catalyzed by molecular metal complexes, *Acc. Chem. Res.* 55 (16) (2022) 2304–2315.
- C. Li, J. Li, L. Qin, P. Yang, D.G. Vlachos, Recent advances in the photocatalytic conversion of biomass-derived furanic compounds, *ACS Catal.* 11 (18) (2021) 11336–11359.
- G. Totaro, L. Sisti, P. Marchese, M. Colonna, A. Romano, C. Gioia, M. Vannini, A. Celli, Current advances in the sustainable conversion of 5-hydroxymethylfurfural to 2,5-furandicarboxylic acid, *ChemSusChem* 15 (2022) e202200501.
- H. Xu, X. Li, W. Hu, Z. Yu, H. Zhou, Y. Zhu, L. Lu, C. Si, Research progress of highly efficient noble metal catalysts for the oxidation of 5-hydroxymethylfurfural, *ChemSusChem* 15 (2022) e202200352.
- H. Liu, W. Jia, X. Yu, X. Tang, X. Zeng, Y. Sun, T. Lei, H. Fang, T. Li, L. Lin, Vitamin C-assisted synthesized Mn-Co oxides with improved oxygen vacancy concentration: boosting lattice oxygen activity for the air-oxidation of 5-(hydroxymethyl)furfural, *ACS Catal.* 11 (2021) 7828–7844.
- L. Luo, Z. Wang, X. Xiang, D. Yan, J. Ye, Selective activation of benzyl alcohol coupled with photoelectrochemical water oxidation via a radical relay strategy, *ACS Catal.* 10 (2020) 4906–4913.
- X. Lu, K.-H. Wu, B. Zhang, J. Chen, F. Li, B.-J. Su, P. Yan, J.-M. Chen, W. Qi, Highly efficient electro-reforming of 5-hydroxymethylfurfural on vertically oriented nickel nanosheet/carbon hybrid catalysts: structure–function relationships, *Angew. Chem. Int. Ed.* 60 (26) (2021) 14528–14535.
- S. Chakraborty, N. Chakraborty, S. Mondal, M. Pal, Band gap engineered Sn-doped bismuth ferrite nanoparticles for visible light induced ultrafast methyl blue degradation, *Ceram. Int.* 48 (24) (2022) 37253–37263.
- C. Yang, C. Laberty-Robert, D. Batuk, G. Cibir, A.V. Chadwick, V. Pimenta, W. Yin, L. Zhang, J.-M. Tarascon, A. Grimaud, Phosphate ion functionalization of perovskite surfaces for enhanced oxygen evolution reaction, *J. Phys. Chem. Lett.* 8 (15) (2017) 3466–3472.
- L. Bai, S. Lee, X. Hu, Spectroscopic and electrokinetic evidence for a bifunctional mechanism of the oxygen evolution reaction, *Angew. Chem. Int. Ed.* 60 (6) (2021) 3095–3103.
- S.K. Pahari, Y.-T. Chen, *In situ* spectroelectrochemical detection of oxygen evolution reaction intermediates with a carboxylated graphene-MnO₂ electrocatalyst, *ACS Appl. Mater. Interfaces* 14 (4) (2022) 5177–5182.
- C. Lang, J. Li, K.R. Yang, Y. Wang, D.a. He, J.E. Thorne, S. Croslow, Q.i. Dong, Y. Zhao, G. Prostko, G.W. Brudvig, V.S. Batista, M.M. Waegele, D. Wang, Observation of a potential-dependent switch of water-oxidation mechanism on Co-oxide-based catalysts, *Chem* 7 (8) (2021) 2101–2117.
- B.M. Hunter, N.B. Thompson, A.M. Müller, G.R. Rossman, M.G. Hill, J.R. Winkler, H.B. Gray, Trapping an iron (VI) water-splitting intermediate in nonaqueous media, *Joule* 2 (2018) 747–763.
- H.B. Tao, Y. Xu, X. Huang, J. Chen, L. Pei, J. Zhang, J. Chen, B.A. Liu, General method to probe oxygen evolution intermediates at operating conditions, *Joule* 3 (2019) 1498–1509.
- Y. Wu, T. Sakurai, T. Adachi, Q. Wang, Alternatives to water oxidation in the photocatalytic water splitting reaction for solar hydrogen production, *Nanoscale* 15 (14) (2023) 6521–6535.
- B. Tan, A.M. Reyes, E. Menéndez-Proupin, S.E. Reyes-Lillo, Y. Li, Z. Zhang, Full-space potential gradient driven charge migration inside BiFeO₃ photocathode, *ACS Energy Lett.* 7 (10) (2022) 3492–3499.
- J. Li, S. Yi, K. Wang, Y. Liu, J. Li, Alkene-catalyzed rapid layer-by-layer thinning of black phosphorus for precise nanomanufacturing, *ACS Nano* 16 (8) (2022) 13111–13122.
- Z. Zhang, B. Tan, W. Ma, B.o. Liu, M. Sun, J.K. Cooper, W. Han, BiFeO₃ Photocathodes for efficient H₂O₂ production via charge carrier dynamics engineering, *Mater. Horiz.* 9 (7) (2022) 1999–2006.
- S.-J. Song, I.S. Raja, Y.B. Lee, M.S. Kang, H.J. Seo, H.U. Lee, D.-W. Han, Comparison of cytotoxicity of black phosphorus nanosheets in different types of fibroblasts, *Biomater. Res.* 23 (2019) 23.
- A. Mukherjee, S. Chakraborty, N. Kumari, W.-N. Su, S. Basu, Visible-light-mediated electrocatalytic activity in reduced graphene oxide-supported bismuth ferrite, *ACS Omega* 3 (2018) 5946–5957.
- R. Kronberg, H. Lappalainen, K. Laasonen, Revisiting the Volmer-Heyrovský mechanism of hydrogen evolution on a nitrogen doped carbon nanotube: constrained molecular dynamics versus the nudged elastic band method, *PCCP* 22 (2020) 10536–10549.
- N.K. Roberts, H.L. Northey, Proton and deuteron mobility in normal and heavy water solutions of electrolytes, *J. Chem. Soc. Faraday Trans.* 70 (1974) 253.
- C. Hu, Y. Hu, C. Fan, L. Yang, Y. Zhang, H. Li, W. Xie, Surface-enhanced Raman spectroscopic evidence of key intermediate species and role of NiFe dual-catalytic center in water oxidation, *Angew. Chem. Int. Ed.* 60 (36) (2021) 19774–19778.
- H. Chen, M. Ikeda-Saito, S. Shaik, Nature of the Fe-O₂ bonding in oxy-myoglobin: effect of the protein, *J. Am. Chem. Soc.* 130 (44) (2008) 14778–14790.
- T.A. Jackson, J.-U. Rohde, M.S. Seo, C.V. Sastri, R. DeHont, A. Stubna, T. Ohta, T. Kitagawa, E. Münck, W. Nam, L. Que, Axial ligand effects on the geometric and electronic structures of nonheme oxoiron(IV) complexes, *J. Am. Chem. Soc.* 130 (37) (2008) 12394–12407.
- D. Wang, K. Ray, M.J. Collins, E.R. Farquhar, J.R. Frisch, L. Gómez, T.A. Jackson, M. Kerscher, A. Waleska, P. Comba, M. Costas, L. Que, Nonheme oxoiron(IV) complexes of pentadentate N5 ligands: spectroscopy, electrochemistry, and oxidative reactivity, *Chem. Sci.* 4 (2013) 282–291.
- B.J. Taitt, D.-H. Nam, K.-S. Choi, A comparative study of nickel, cobalt, and iron oxyhydroxide anodes for the electrochemical oxidation of 5-hydroxymethylfurfural to 2,5-furandicarboxylic Acid, *ACS Catal.* 9 (1) (2019) 660–670.
- J. Du, D. Xiang, K. Zhou, L. Wang, J. Yu, H. Xia, L. Zhao, H. Liu, W., Zhou Electrochemical hydrogen production coupled with oxygen evolution, organic synthesis, and waste reforming, *Nano Energy* 104 (2022), 107875.
- C. Zhou, W. Shi, X. Wan, Y. Meng, Y. Yao, Z. Guo, Y. Dai, C. Wang, Y. Yang, Oxidation of 5-hydroxymethylfurfural over a magnetic iron oxide decorated rGO supporting Pt nanocatalyst, *Catal. Today* 330 (2019) 92–100.
- B. You, X.uan Liu, N. Jiang, Y. Sun., A General Strategy for Decoupled Hydrogen Production from Water Splitting by Integrating Oxidative Biomass Valorization, *J. Am. Chem. Soc.* 138 (2016) 13639–13646.
- C. Ding, W. Qin, N. Wang, G. Liu, Z. Wang, P. Yan, J. Shi, C. Li, Solar-to-hydrogen efficiency exceeding 2.5% achieved for overall water splitting with an all earth-abundant dual-photoelectrode, *PCCP* 16 (2014) 15608.

***In Situ* Observation of Photoelectrochemical Water Oxidation Intermediates for Selective Biomass Upgrading with Simultaneous Hydrogen Production**

Sandip K. Pahari^{a,b,c} and Yit-Tsong Chen^{a,b,c,*}

^aDepartment of Chemistry, National Taiwan University, Taipei 10617, Taiwan

^bInstitute of Atomic and Molecular Sciences, Academia Sinica, Taipei 10617, Taiwan

^cDepartment of Electrophysics, PSMC-NYCU Research Center, and LIGHTMED Laser System Research Center, National Yang Ming Chiao Tung University, Hsinchu 300093, Taiwan

*Corresponding author. Email: ytc22@nycu.edu.tw

Table of Contents

Section A. Experimental Methods	S2
Section B. Structural Determination and Surface Area Analysis	S4
Section C. Photoelectrochemical Measurements	S7
Section D. Biomass Conversion	S12
Table S1 Comparison of the HER Performance for Different Catalysts	S20
Table S2 Comparison of the OER Performance for Different Catalysts	S21
Table S3 Electrocatalytic performances of the recently reported electrocatalysts for the HMF oxidation to FDCA	S22
References	S23

Section A. Experimental Methods

● Chemicals

Bismuth nitrate pentahydrate $[\text{Bi}(\text{NO}_3)_3 \cdot 5\text{H}_2\text{O}]$, iron (III) nitrate nonahydrate $[\text{Fe}(\text{NO}_3)_3 \cdot 9\text{H}_2\text{O}]$, citric acid, and N-methyl-2-pyrrolidone (NMP) were purchased from Alfa Aesar. Bulk black phosphorus crystal (purity > 99.995%) was obtained from SMT Metalle Wimmer, Austria.

● Synthesis of bismuth ferrite (BFO) nanosheets

In the synthesis of bismuth ferrite (BiFeO_3 , denoted by BFO), 0.1 M $\text{Bi}(\text{NO}_3)_3 \cdot 5\text{H}_2\text{O}$ and 0.1 M $\text{Fe}(\text{NO}_3)_3 \cdot 9\text{H}_2\text{O}$ were added to 5 mL of a 0.5 M HNO_3 solution. Subsequently, 2 mL of 0.2 M citric acid in 5 mL deionized water was added to the above mixture. The mixture was stirred at room temperature for 2 hr and then dried at 120 °C. Finally, the obtained powder was calcined at 550 °C for 2 hr.

● Synthesis of few-layer phosphorene (FLP) from black phosphorus (BP)

FLP was prepared from the liquid-phase exfoliation of bulk black phosphorus (BP) using NMP as a solvent. In a typical process, large BP crystal was grounded into small sizes with a mortar pestle. Then, 10 mg of the grounded BP was added to 20 ml of degassed NMP and stirred in an argon (Ar) atmosphere for 6 hr to intercalate the solvent molecules into the BP interlayers for better exfoliation. Subsequently, the FLP-containing solution was ultrasonicated for 2 hr using a probe sonicator. During the ultrasonication for dispersion, the temperature was kept below 10 °C controlled by an ice bath. Finally, the dispersion was centrifuged at 1000 rpm for 5 min to remove the non-exfoliated bulk BP.

● Few-layer phosphorene with surface modification of phosphate groups (FLP-P)

The as-prepared FLP (from the above synthesis) was oxidized in air at 50 °C for 30 min to form FLP-P.

- **Synthesis of FLP-BFO nanosheets**

In a typical synthesis process of FLP-P-BFO nanosheets, 10 mg of BP was grounded to small pieces, followed by adding 20 ml of NMP and stirring in an Ar atmosphere for 2 hr. The solution was then ultrasonicated for 2 hr using a probe sonicator. Subsequently, the FLP-containing solution was centrifuged at 1000 rpm for 5 min to remove the non-exfoliated bulk BP. Afterwards, 10 mg of the as-synthesized BFO was added to the FLP-containing solution and ultrasonicated for 30 min, followed by stirring the solution mixture in an Ar atmosphere for 12 hr. After the reaction, the dispersion was filtered, washed with ethanol, and then heated at 80 °C in N₂ atmosphere for 1 hr to remove the solvent.

- **Synthesis of FLP-P-BFO nanosheets**

After the as-prepared FLP-BFO nanosheets (from the above synthesis), the FLP-BFO sample was heated at 50 °C in air for 30 min to form FLP-P-BFO.

Section B. Structural Determination and Surface Area Analysis

• Spectroscopic and electron microscopic characterizations

High-resolution transmission electron microscopy (HR-TEM) images were obtained in a TEM (JEOL, JEM-2100F) with an acceleration voltage of 200 kV. Raman spectra of the as-synthesized electrocatalysts were recorded in a Raman spectrometer (NT-MDT, NTEGRA Spectra) equipped with an 1800 gr mm^{-1} grating and a 488-nm laser as an excitation source. Fourier-transform infrared (FTIR) spectra were scanned in a Horiba, FT720 spectrophotometer. X-ray photoelectron spectroscopy (XPS) measurements were conducted using an ESCA photoelectron spectrometer (Ulvac-PHI 1600) with the photon energy of $1486.6 \pm 0.2\text{ eV}$ (Al $K\alpha$ radiation). The binding energies of the observed XPS signals were calibrated against the carbon C 1s peak at 284.8 eV. The Shirley-Sherwood method was employed to subtract the background.

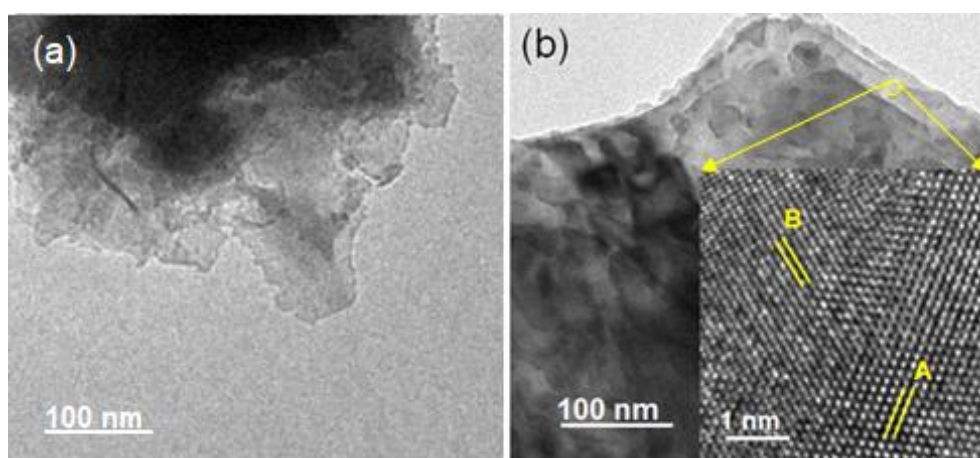


Figure S1. (a) The TEM image of FLP presents its thin-layer structure. (b) The TEM image of FLP-BFO nanosheets shows that FLP is stacked with BFO nanosheets. The right lower inset displays the HR-TEM image of two distinctive crystal fringes with the interplanar separations of 0.26 nm (marked by A) and 0.23 nm (labelled by B), corresponding to the FLP and BFO crystal structures, respectively.

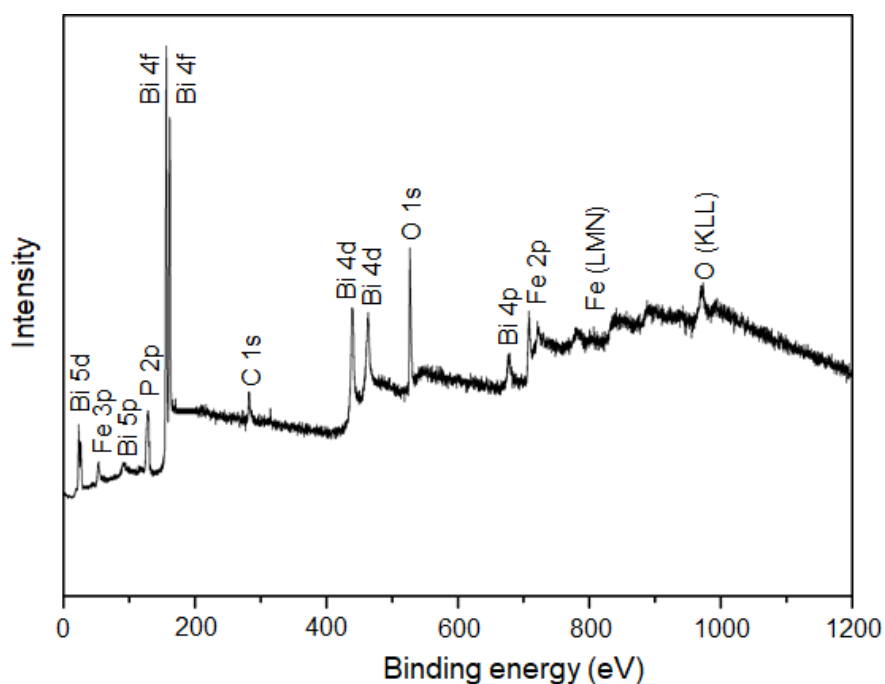


Figure S2. The XPS survey spectrum of the as-prepared FLP-P-BFO hybrid photocatalyst.

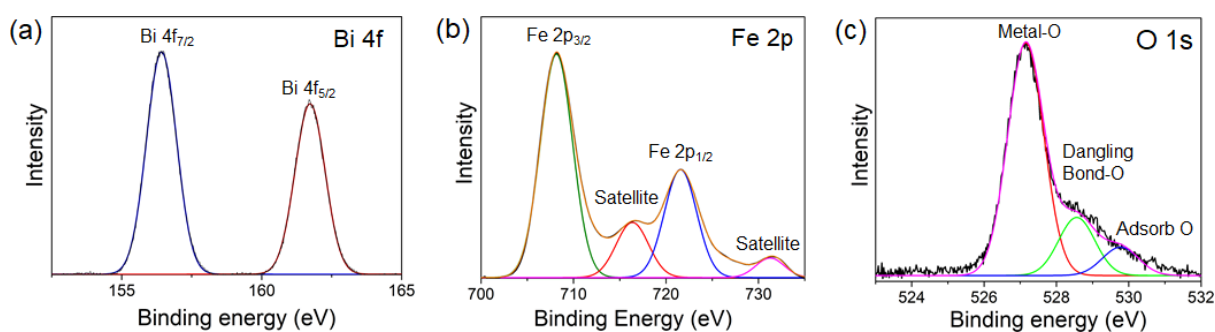


Figure S3. The XPS spectra of (a) Bi 4f, (b) Fe 2p, and (c) O 1s of the as-prepared FLP-P-BFO hybrid photocatalyst were observed and analyzed. (a) The Bi 4f spectrum shows the characteristic binding energies of the Bi^{3+} state at 156.4 and 161.7 eV. (b) In the Fe 2p spectrum, the bands at 708.2 and 721.6 eV are the Fe $2p_{3/2}$ and Fe $2p_{1/2}$ doublets of Fe^{3+} , respectively; the adjacent signals at 716.4 and 731.4 eV represent their satellite peaks. (c) The signals in the O 1s spectrum at 527.1, 528.6, and 529.8 eV correspond to the iron-oxygen bond (Fe–O), the surface dangling bond ($\text{O}\cdot$), and the adsorbed oxygen (O_2 and/or H_2O), respectively.

- **Surface area analysis with the Brunauer-Emmett-Teller (BET) method**

The surface areas of the as-prepared photoelectrodes were measured with the Brunauer-Emmett-Teller (BET) method and analyzed using a Quantachrome Autosorb-6 instrument. For the BET analysis, samples were degassed at 150 °C for 12 hr and subjected to the N₂ adsorption-desorption at 77 K.

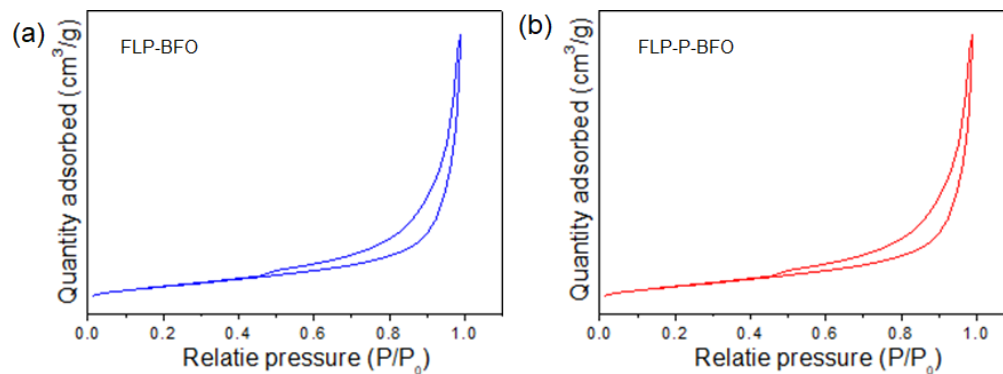


Figure S4. The N₂ adsorption-desorption isotherms of (a) FLP-BFO and (b) FLP-P-BFO were measured for comparison. The surface areas of FLP-BFO and FLP-P-BFO were determined to be 55.6 and 55.8 m² g⁻¹, respectively.

Section C. Photoelectrochemical Measurements

● Fabrication of FLP-P, BFO, FLP-BFO, and FLP-P-BFO photoelectrodes

Electrochemical measurements were performed using carbon cloth substrates ($1 \times 2 \text{ cm}^2$). Prior to electrochemical measurements, the carbon cloth substrates were washed consecutively with acetone, 1 M HNO_3 , and deionized water to thoroughly remove surface impurities. The photoelectrode materials were deposited on the carbon cloth via the drop casting method. In the process, the photoelectrode materials were dispersed in Nafion, then deposited in the area of $1 \times 1 \text{ cm}^2$ on carbon cloth, and finally dried under vacuum at $60 \text{ }^\circ\text{C}$.

● Photoelectrochemical (PEC) measurements

The PEC measurements were carried out on the electrochemical station of a three-electrode system. A 200-W LED-based solar simulator was used as the illumination source. The characteristics of photoelectrodes were tested by the current vs. potential (I-V) scans, chronoamperometry, cyclic voltammetry (CV), Mott-Schottky plots, and electrochemical impedance spectroscopy (EIS) using an Autolab with the NOVA 2.1 software. The EIS measurements were characterized in an open-circuit condition with the frequency range of 10^{-2} – 10^5 Hz. In the measuring process, a saturated calomel electrode (SCE), a Pt wire, and the prepared photoelectrode (i.e., the FLP-P, BFO, FLP-BFO, or FLP-P-BFO photoelectrode) were used as the reference, counter, and working electrodes, respectively. Aqueous solution of 0.5 M Na_2SO_4 at pH 7.0 was used as an electrolyte.

All electrochemical potentials mentioned in this work have been converted to the potential vs. RHE (in volts) according to Eq. (1)

$$E_{\text{RHE}} = E_{\text{Ag/AgCl}} + E_{\text{Ag/AgCl vs. NHE}} + 0.059 \text{ pH} \quad (1)$$

where $E_{\text{Ag/AgCl vs. NHE}} = 0.197 \text{ V}$ at $20 \text{ }^\circ\text{C}$. Prior to all PEC measurements, N_2 gas was purged in the solution to remove any dissolved O_2 , therefore suppressing the reduction of O_2 at the counter electrode. A mask was applied to the electrode with an aperture of $1 \times 1 \text{ cm}^2$. The

electrode was then illuminated through the aperture ($1 \times 1 \text{ cm}^2$) with a 200-W LED-based solar simulator of adjustable power settings.

The Mott-Schottky measurements were carried out in the dark condition. The Mott-Schottky plot was evaluated using the following Eq. (2).

$$\frac{1}{C^2} = \frac{2}{N_D e \epsilon_0 \epsilon} \left[(V - V_{FB}) - \frac{k_B T}{e} \right] \quad (2)$$

where C is the space charge layer capacitance, N_D is the concentration of charger carriers, ϵ is the dielectric constant of the material, ϵ_0 is the permittivity of vacuum, e is the elemental charge, V is the applied potential, V_{FB} is the flat band potential, k_B is Boltzmann's constant, and T is the absolute temperature.

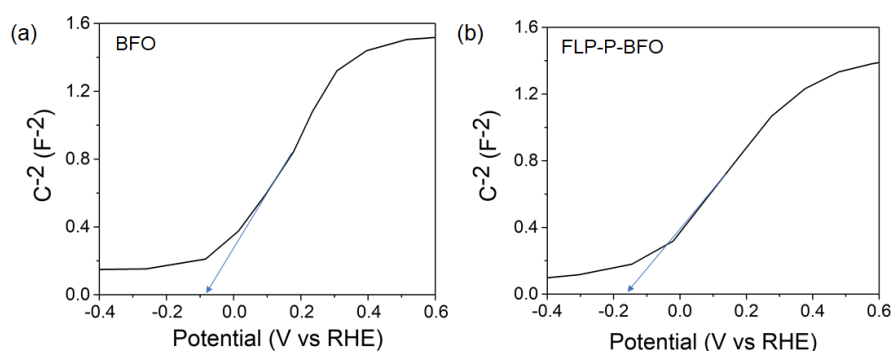


Figure S5. The Mott-Schottky plots for (a) BFO and (b) FLP-P-BFO were measured in 0.5 M Na_2SO_4 solution.

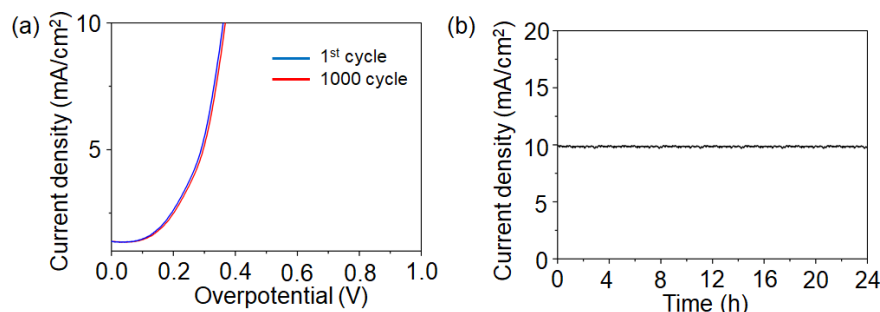


Figure S6. In the FLP-P-BFO-catalytic OER using 0.5 M Na_2SO_4 solution as an electrolyte, (a) the polarization curves exhibit a negligible change after running 1000 cycles and (b) the chronoamperometric response at 10 mA cm^{-2} displays very little attenuation within 24 h.

- **Electrochemically active surface area (ECSA) determination**

The ECSA of a catalyst was calculated from the electrochemical double-layer capacitance of the catalytic sample. The electrochemical capacitance was determined by measuring the non-faradaic capacitive current associated with the double-layer charging from the scan-rate dependence of cyclic voltammograms (CV). The ECSA of a catalyst was calculated by

$$ECSA = C_{dl}/C_s$$

where C_{dl} is the electrochemical double-layer capacitance of the sample and C_s stands for the specific capacitance of a standard electrode material with a unit surface area. This value describes the capacitance of an ideal flat catalyst surface. Ideally, one would synthesize every catalyst with smooth, planar surface and measure its C_s to estimate ECSA; however, this is not practical for most electrodeposited systems. Here, according to the C_s values of the carbon electrode materials reported in the literature, 0.02 mF cm^{-2} was taken for the ECSA calculation. The double-layer charging current (i_c) equals to the product of the scan rate (ν) and the electrochemical double-layer capacitance (C_{dl})

$$i_c = \nu C_{dl}$$

Therefore, a plot of i_c as a function of ν yields a straight line with the slope of C_{dl} (Fig. S7). The unit of ECSA was converted from cm^2 to $\text{m}^2 \text{ g}^{-1}$. Consequently, the ECSAs of the FLP-BFO and FLP-P-BFO electrodes were determined to be 10.45 and $10.49 \text{ m}^2 \text{ g}^{-1}$, respectively.

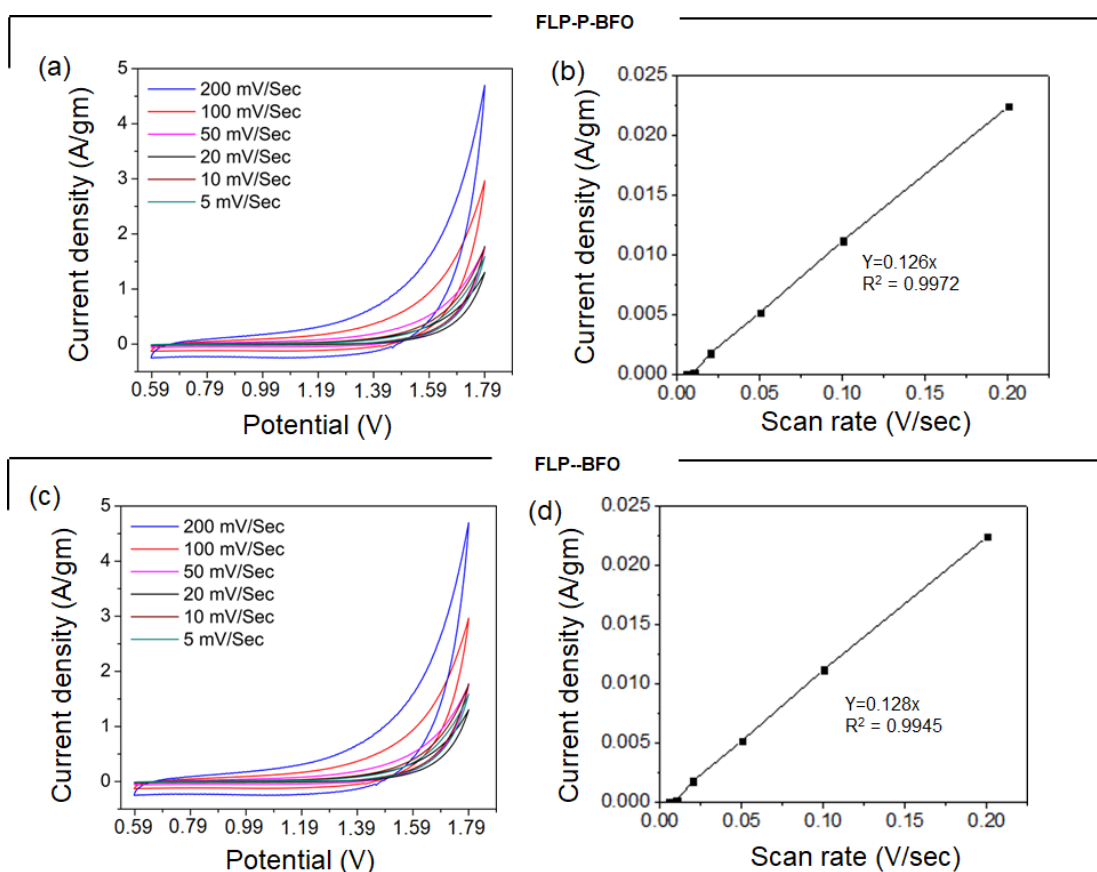


Figure S7. The current-voltage (CV) curves of the (a) FLP-P-BFO and (c) FLP-BFO electrocatalysts were measured at different scan rates in a 0.5 M Na₂SO₄ electrolyte. (b, d) The current density vs. scan rate plots are presented for (a, c), respectively, in which the current densities were taken from the non-faradic region of the CV plot at 0.99 V (vs RHE).

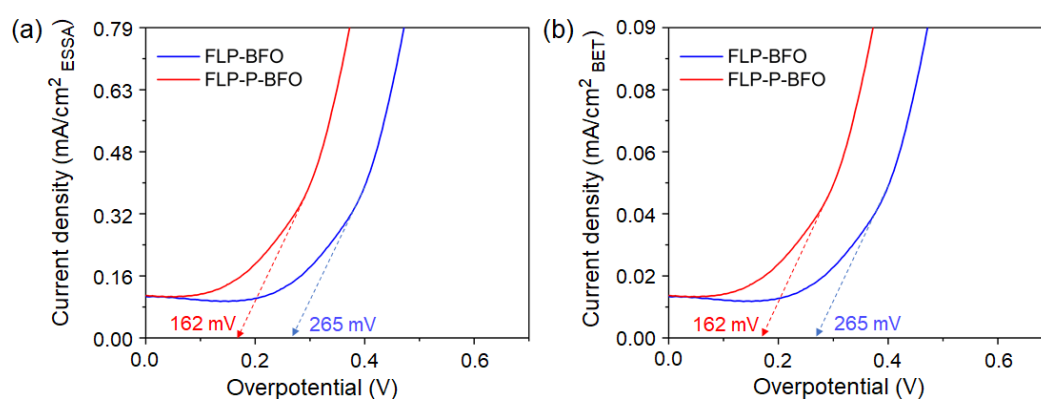


Figure S8. The LSV curves are normalized with respect to the (a) ECSA and (b) BET surface areas. The overpotentials keep the same as those measured in Fig. 3d of the main text.

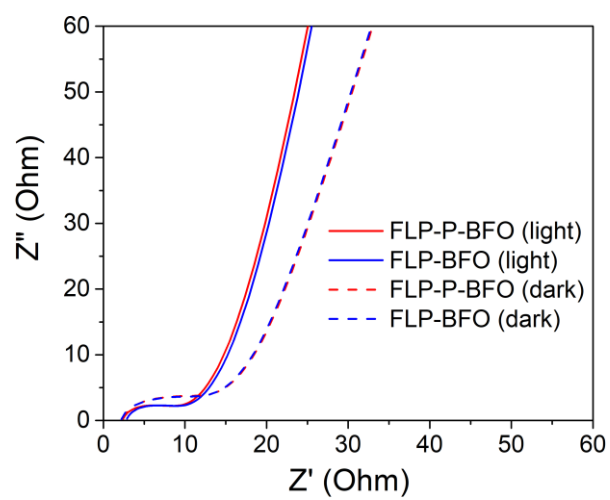


Figure S9. The EIS curves of the FLP-BFO and FLP-P-BFO electrocatalysts were measured separately under visible-light illumination and in the dark condition.

Section D. Biomass Conversion

The photoelectrochemical oxidation of HMF to FDCA was performed with a three-electrode system in an Autolab potentiostat with the NOVA 2.1 software. The as-prepared FLP-P-BFO was used as the working electrode, an Ag/AgCl (sat. KCl) electrode as the reference electrode, and a Pt wire as the counter electrode. All the potentials reported herein were calibrated with respect to the reversible hydrogen electrode (RHE). The experiments of the HMF oxidation to FDCA were conducted in 10 mL 0.5 M Na₂SO₄ solution, with or without 5 mM HMF at room temperature. To eliminate the interference from O₂ in the electrocatalytic oxidation reaction, N₂ gas was bubbled through the solution for 20 min before the reaction. The test was performed at a cell voltage of 1.39 V vs. RHE. The scan rate for all current-voltage (CV) measurements was set to 10 mV s⁻¹. Again, all potentials mentioned in this work were converted to the potential vs. RHE (in volts). For visible-light excitation, a 200-W LED-based solar simulator was used as the illumination source.

After the biomass conversion reaction, the products were analyzed by gas chromatography-mass spectrometry (GC-MS), which comprises a gas chromatograph, equipped with an HT-5MS column (Agilent, length: 30 m, internal diameter: 0.22 mm, and film thickness: 0.25 μm), and a quadrupole mass detector. Helium (He) was used as the carrier gas at the flow rate of 1 mL min⁻¹. The oven was programmed to start at 40 °C and increase at the rate of 15 °C min⁻¹ until 310 °C. During the PEC-catalytic oxidation of HMF, 100 μL of aliquot was taken from the reaction mixture with 10-min time interval. The aliquots were analyzed by GC-MS to inspect the formations of both intermediates and products during the progress of the reaction.

The concentrations of the consumed HMF and generated products in the anodic compartment were measured by high-performance liquid chromatography (HPLC). The HPLC was equipped with an ultraviolet-visible detector (with the absorption wavelength of 265 nm)

and a Shim-pack GWS C18 5 μm column (length: 250 mm and internal diameter: 4.6 mm). The eluent solvent is a mixture of an aqueous solution of 5 mM ammonium formate and methanol (with the ratio of 1:3). 10 μL of the reactant solution was injected for HPLC analysis. The HMF conversion together with the yield of the oxidation product for producing FDCA were calculated from the following equations.

$$\text{Conversion (\%)} = \frac{\text{mol of HMF consumed}}{\text{mol of initial HMF}} \times 100\%$$

$$\text{Yield (\%)} = \frac{\text{mol of product formed}}{\text{mol of initial HMF}} \times 100\%$$

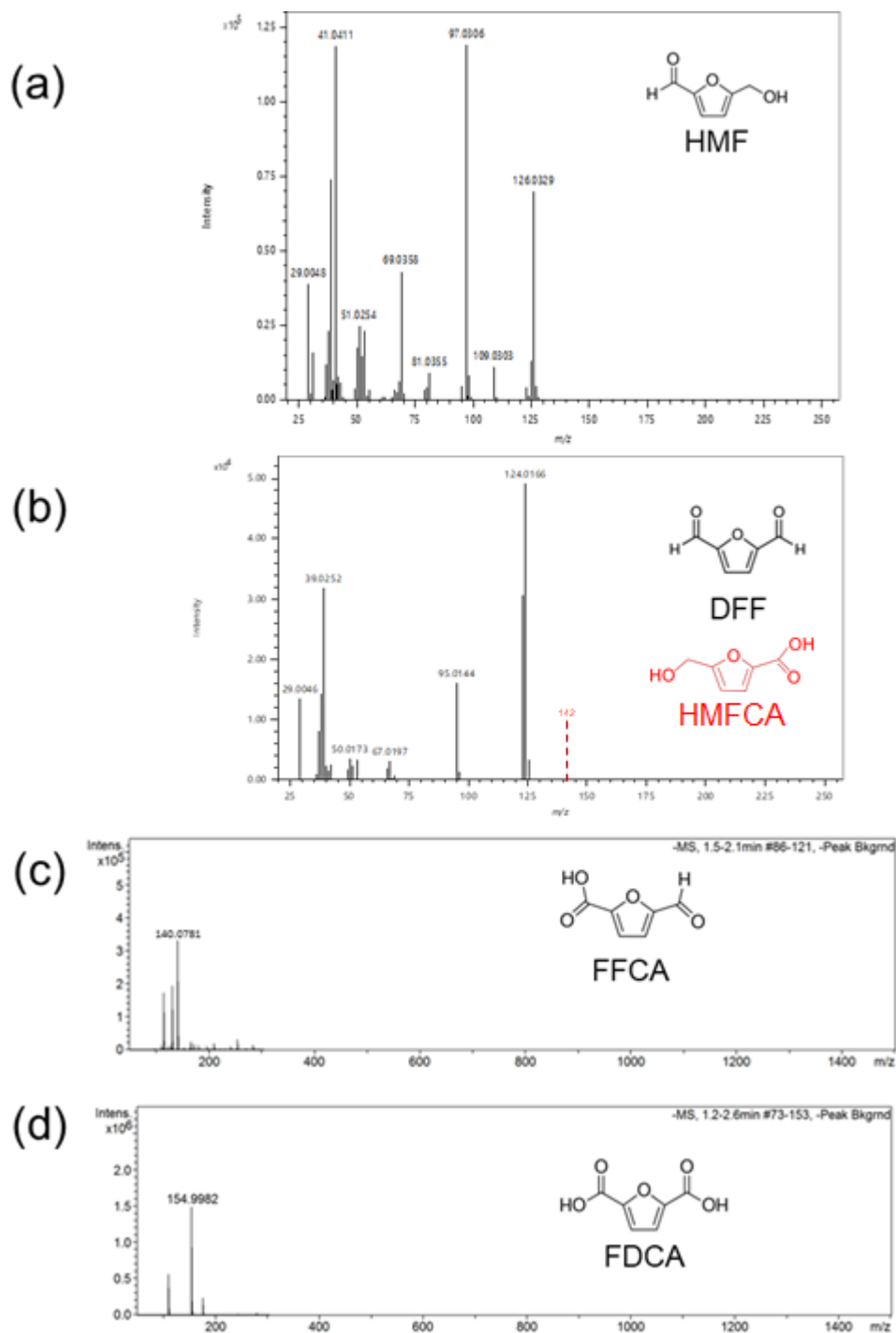


Figure S10. The mass spectra of (a) hydroxymethylfurfural (HMF), (b) 2,5-diformylfuran (DFF), (c) 5-formyl-2-furancarboxylic acid (FFCA), and (d) furandicarboxylic acid (FDCA) were detected in the GC-MS analyses. During the HMF conversion reaction, DFF and FFCA were formed as intermediates. In (b), the vertical red dotted line is supposed to be the peak position (at $m/z = 142$) of the parent ion of 5-hydroxymethyl-2-furoic acid (HMFCa), if

HMFCFA would appear. The absence of the signal at $m/z = 142$ indicates that HMFCFA was not formed during the HMF oxidation process.

- **The conversion reactions of HMF to FDCA with different catalytic methods:**

- (a) electrocatalysis, (b) photocatalysis, and (c) PEC catalysis**

The HMF conversion to FDCA via different catalytic routes was examined with the results displayed in Fig. S11 and the detailed experimental conditions and procedures discussed below.

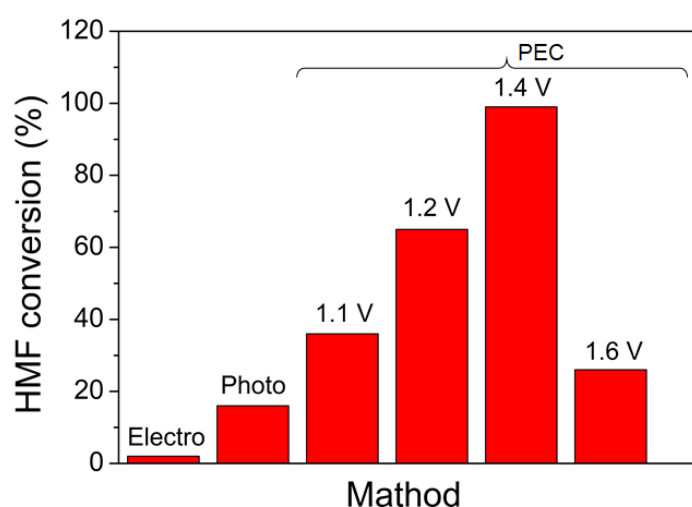


Figure S11. A comparison of the HMF conversion to FDCA (after 90-min reaction) with different catalytic methods. (a) Electrocatalysis (denoted by Electro) was carried out at 1.4 V vs. RHE. (b) Photocatalysis (denoted by Photo) was performed with the visible-light illumination of 50 mW cm^{-2} . (c) Photoelectrochemical catalysis (denoted by PEC) was conducted with the visible-light illumination of 50 mW cm^{-2} and at various electrochemical potentials.

- (a) Electrocatalysis**

The electrocatalytic HMF oxidation reaction was carried out using the same electrochemical setup as our standard PEC-catalytic HMF oxidation experiment, but without shining visible light during the reaction. The anode, cathode, and reference electrodes were the

FLP-P-BFO electrocatalyst deposited on carbon cloth, Pt, and Ag/AgCl, respectively. In the electrocatalytic reaction, 5 mM HMF was used as a reactant and 0.5 M Na₂SO₄ was used as an electrolyte. The experiment was carried out at 1.4 V vs. RHE.

(b) Photocatalysis

In the photocatalytic HMF oxidation reaction, the experimental conditions (such as the electrocatalyst, electrolyte, and reactant used) are the same as those of (a) Electrocatalysis. However, instead of applying electricity, the FLP-P-BFO electrocatalyst deposited on carbon cloth was illuminated with a 200-W LED-based solar simulator of 50 mW cm⁻².

(c) Photoelectrochemical catalysis

The PEC-catalytic HMF oxidation reaction was conducted with the same experimental conditions (such as the electrocatalyst, electrolyte, and reactant used) as those in the above (a) Electrocatalysis and (b) Photocatalysis. However, in this (c) PEC catalysis, both illumination (with a 200-W LED-based solar simulator of 50 mW cm⁻²) and electricity were applied (with the potentials of 1.1, 1.2, 1.4, and 1.6 V, respectively) for the HMF oxidation reaction. The maximal conversion rate of the HMF oxidation to FDCA was found when the electrochemical potential was adjusted to 1.4 V. This outcome is consistent with the *in situ* Raman spectroscopic finding in the PEC-assisted FLP-P-BFO-catalytic water oxidation reaction (as displayed in Fig. 4 of the main text). As shown in Fig. 4, applying the electrochemical potential of 1.39 V can reach the maximal production of the Fe-OOH intermediate, which is proved predominant in the HMF conversion to FDCA (in Fig. 5c and the related context in the main text).

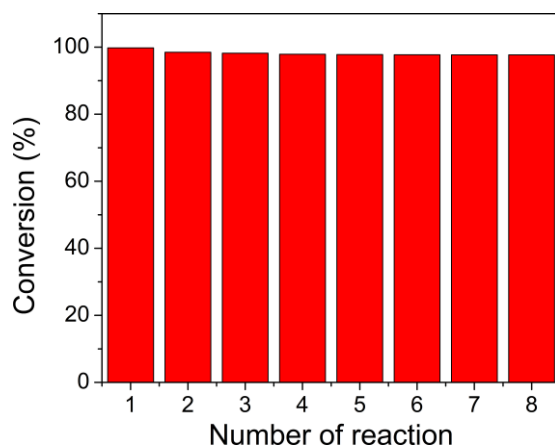


Figure S12. In the FLP-P-BFO-catalytic HMF conversion to FDCA, the anodic conversion efficiency was measured for eight consecutive cycles of the HMF oxidation, where 10 mM HMF was added to the 0.5 M Na₂SO₄ electrolyte and the electrical potential was set at 1.4 V.

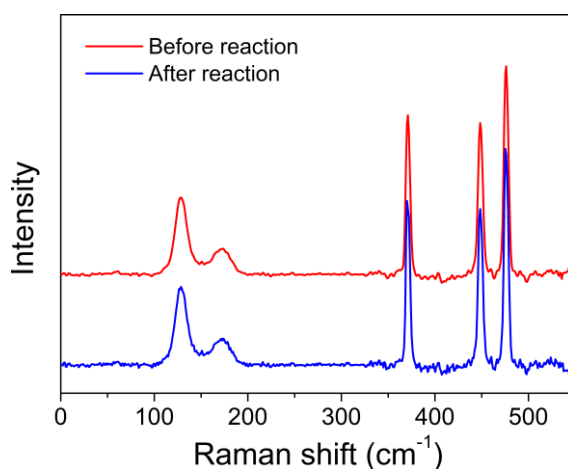


Figure S13. In the FLP-P-BFO-catalytic HMF conversion to FDCA, the excellent electrocatalytic durability of the FLP-P-BFO electrode was demonstrated by examining the Raman spectra of the FLP-P-BFO photocatalyst before and after the eight HMF conversion reactions.

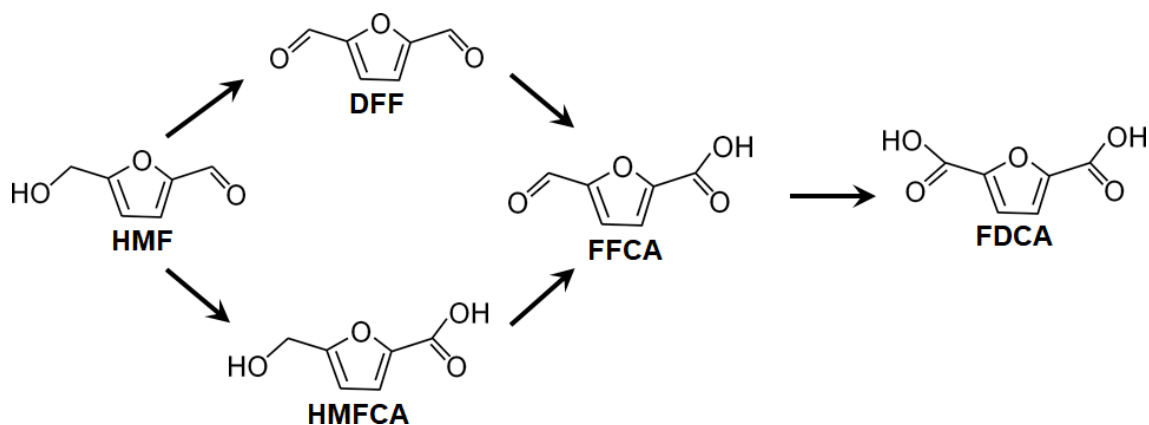


Figure S14. Different intermediates (DFF and HMFCFA) are involved in the two possible pathways for the HMF oxidation to FDCA. Nevertheless, both pathways converge toward the formation of FFCA prior to FDCA.

- **Description of a two-electrode setup**

To establish a two-electrode system, a traditional H-type cell with FLP-P-BFOs as a working electrode was used for both photocathode and photoanode (Fig. S15). In the cell, the cathode and anode electrodes were immersed in two separate compartments, which are connected through a proton exchange membrane (PEM). For PEC experiments, the cathode and anode electrodes were illuminated separately by a 200-W LED-based solar simulator. When a potential was applied (1.39 V vs. RHE) at the anode, water was oxidized to the OER intermediates, protons, and electrons. The electrons transported to the cathode via an external circuit. The OER intermediates oxidized HMF to FDCA. The protons transferred to the cathode compartment through the PEM membrane and were reduced to H₂.

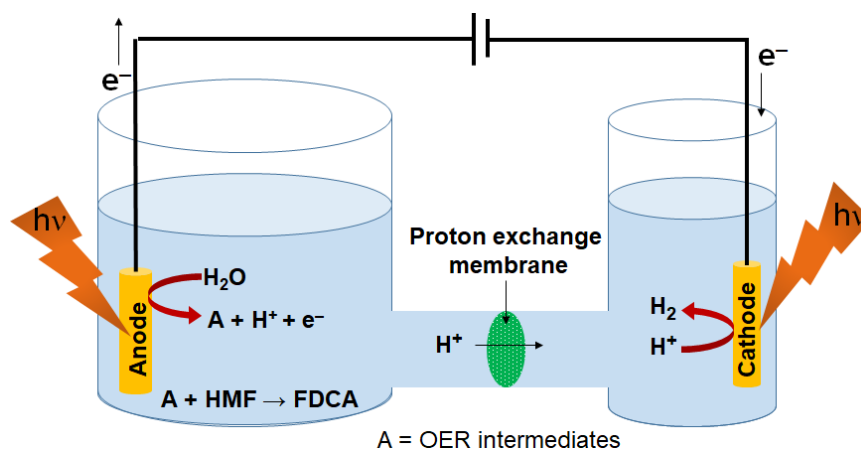


Figure S15. Schematic illustration of an H-type cell for the two-electrode system using FLP-P-BFO as both photocathode and photoanode.

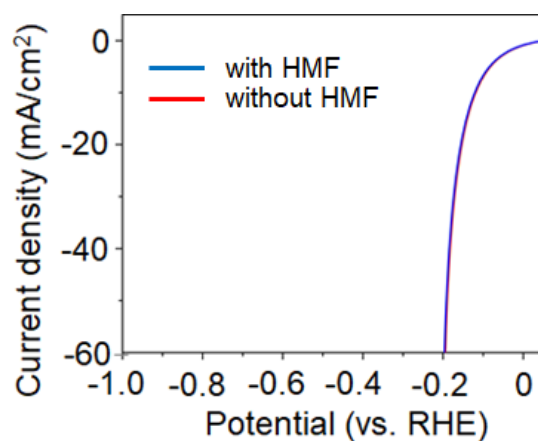


Figure S16. The LSV curves of the FLP-P-BFO-catalytic HER were measured at the scan rate of 10 mV s^{-1} in $0.5 \text{ M Na}_2\text{SO}_4$ solution with, or without, introducing 10 mM HMF .

Table S1. Comparison of the HER Performance for Different Catalysts

Catalysts	Overpotential (mV) at 10 mA cm⁻² current density	Electrolyte	Light flux (mW cm⁻²)	References
FLP-P-BFO	110	0.5 M Na ₂ SO ₄	50	This work
few-atomic-layers iron (Fe _{FAL}) anchored on GaN nanowire arrays	~200	0.5 M KHCO ₃ aqueous solution	100	1
Cobalt Phosphide (CoP)	230	0.5 M sulfuric acid	76	2
P@MoS ₂	134	0.5 M sulfuric acid	2.4	3
palladium doped 1T-phase molybdenum disulfide–black phosphorene	152	0.5 M sulfuric acid	100	4
Mn–FeP/Co ₃ (PO ₄) ₂	117	1 M PBS	-	5
phosphorene quantum dot/prussian blue	148	Neutral pH	-	6
Iron phosphorus oxide	300	1 M PBS	-	7
Phosphate- decorated Ni ₃ Fe- LDHs@CoP _x	370	1 M phosphate buffer + 0.5 M NaCl	-	8
Fe@N-CNT/IF	525	0.5 M Na ₂ SO ₄	-	9

Table S2. Comparison of the OER Performance for Different Catalysts

Catalysts	Overpotential (mV) at 10 mA cm⁻² current density	Electrolyte	Light flux (mW cm⁻²)	References
FLP-P-BFO	162	0.5 M Na ₂ SO ₄	50	This work
N, Fe–CoS ₂ nanorods	215	1 M KOH	100	10
Fluorine-doped FeOOH	270	1 M NaOH	100	11
Crystalline Fe ₂ O ₃ /Fe ₂ TiO ₅	350	1 M NaOH	100	12
Amorphous Cobalt– Iron Hydroxide Nanosheet	280	1 M KOH	100	13
porous Sn-doped iron oxide	330	1 M KOH	100	14
Iron-Treated NiO	500	1 M KOH	38.6	15

Table S3. Electrocatalytic performances of the recently reported electrocatalysts for the HMF oxidation to FDCA

Catalysts	Oxidation potential (V) at 10 mA cm⁻² current density	Conversion (%)	Selectivity (%)	Reference
FLP-P-BFO	1.39	100	100	This work
NiCoFe LDHs	1.51	95.5	84.9	16
d-NiFe LDH	1.47	97.3	96.8	17
Ni(OH) ₂ -NiFeP	1.55	100	99	18
FeP-NiMoP ₂	1.404	100	99.2	19
MoO ₂ -FeP	1.424	100	98.6	20
(FeCrCoNiCu) ₃ O ₄	1.5	-	98	21

References

1. B. Zhou, P. Ou, R. T. Rashid, S. Vanka, K. Sun, L. Yao, H. Sun, J. Song, Z. Mi, Few-atomic-layers iron for hydrogen evolution from water by photoelectrocatalysis, *iScience* 23 (2020) 101613.
2. T. R. Hellstern, J. D. Benck, J. Kibsgaard, C. Hahn, T. F. Jaramillo, Engineering Cobalt Phosphide (CoP) Thin Film Catalysts for Enhanced Hydrogen Evolution Activity on Silicon Photocathodes, *Adv. Energy Mater.* 6 (2016) 1501758.
3. T. D. Munusamy, M. R. Khan, S. Y. Chin, Photoelectrochemical performance of P@MoS₂ for hydrogen evolution reaction, *Materials Today: Proceedings* 48 (2022) 766–770.
4. X. Song, B. Li, W. Peng, C. Wang, K. Li, Y. Zhu, Y. Mei, A palladium doped 1T-phase molybdenum disulfide–black phosphorene two-dimensional van der Waals heterostructure for visible-light enhanced electrocatalytic hydrogen evolution, *Nanoscale* 13 (2021) 5892–5900.
5. H. Liu, X. Peng, X. Liu, G. Qi, J. Luo, Porous Mn-Doped FeP/Co₃(PO₄)₂ Nanosheets as Efficient Electrocatalysts for Overall Water Splitting in a Wide pH Range, *ChemSusChem* 12 (2019) 1334-1341.
6. X. Xia, L. Liu, X. Li, S. Gao, T. Yang, Highly efficient electrocatalytic hydrogen evolution over edge-modified phosphorene quantum dot/prussian blue skeleton structure, *J. Catal.* 374 (2019) 401-408.
7. D. Cao, B. Sheng, Z. Qi, W. Xu, S. Chen, O. A. Moses, R. Long, Y. Xiong, X. Wu, L. Song, Self-optimizing iron phosphorus oxide for stable hydrogen evolution at high current, *App. Cat. B: Environ.* 298 (2021) 120559.
8. L. X. Zhao, M. G. Sendeku, X. Zhang, L. Xu, Z. Wang, S. Wang, X. Duan, H. Liu, W. Liu, D. Zhou, H. Xu, Y. Kuang, X. Sun, Phosphate-decorated Ni₃Fe-LDHs@CoPx nanoarray for near-neutral seawater splitting, *Chem. Eng. J* 460 (2023) 141413.
9. J. Yu, G. Li, H. Liu, L. Zeng, L. Zhao, J. Jia, M. Zhang, W. Zhou, H. Liu, Y. Hu, Electrochemical Flocculation Integrated Hydrogen Evolution Reaction of Fe@N-Doped Carbon Nanotubes on Iron Foam for Ultralow Voltage Electrolysis in Neutral Media, *Adv. Sci.* 6 (2019) 1901458.
10. J. Lu, L. Cai, N. Zhang, B. Qiu, Y. Chai, Robust Photoelectrochemical oxygen evolution with N, Fe–CoS₂ nanorod arrays, *ACS Appl. Mater. Interfaces* 11 (2019) 44214–44222.
11. Efficient photoelectrochemical water oxidation on hematite with fluorine-doped FeOOH and FeNiOOH as dual cocatalysts, J. Deng, Q. Zhang, K. Feng, H. Lan, J. Zhong, M. Chaker, D. Ma, *ChemSusChem* 11 (2018) 3783 – 3789.

12. P. S. Bassi, R. P. Antony, P. P. Boix, Y. Fang, J. Barber, L. H. Wong, Crystalline Fe₂O₃/Fe₂TiO₅ heterojunction nanorods with efficient charge separation and hole injection as photoanode for solar water oxidation *Nano Energy* 22 (2016) 310-318.
13. W. Liu, H. Liu, L. Dang, H. Zhang, X. Wu, B. Yang, Z. Li, X. Zhang, L. Lei, S. Jin, Amorphous Cobalt–Iron Hydroxide Nanosheet Electrocatalyst for Efficient Electrochemical and Photo-Electrochemical Oxygen Evolution, *Adv. Funct. Mater.* 27 (2017) 1603904.
14. X. Lv, I. Rodriguez, C. Hu, J. Shang, Modulated anodization synthesis of Sn-doped iron oxide with enhanced solar water splitting performance, *Mater. Today Chem.* 12 (2019) 7e158.
15. B. Mei, A. A. Permyakova, R. Frydendal, D. Bae, T. Pedersen, P. Malacrida, O. Hansen, I. E. L. Stephens, P. C. K. Vesborg, B. Seger, I. Chorkendorff, Iron-Treated NiO as a Highly Transparent p-Type Protection Layer for Efficient Si-Based Photoanodes, *J. Phys. Chem. Lett.* 20 (2014) 3456–3461.
16. M. Zhang, Y. Liu, B. Liu, Z. Chen, H. Xu, K. Yan, Trimetallic NiCoFe-layered double hydroxides nanosheets efficient for oxygen evolution and highly selective oxidation of biomass-derived 5-hydroxymethylfurfural, *ACS Catal.* 10 (2020) 5179- 5189.
17. Y-F. Qi, K-Y. Wang, Y. Sun, J. Wang, C. Wang, Engineering the electronic structure of NiFe layered double hydroxide nanosheet array by implanting cationic vacancies for efficient electrochemical conversion of 5-hydroxymethylfurfural to 2,5-furandicarboxylic acid, *ACS Sustain Chem Eng.* 10 (2021); 10, 645- 654.
18. R. Luo, Y. Li, L. Xing, N. Wang, R. Zhong, Z. Qian, C. Du, G. Yin, Y. Wang, L. Du, A dynamic Ni(OH)₂-NiOOH/NiFeP heterojunction enabling high-performance E-upgrading of hydroxymethylfurfural, *Appl Catal B.* 311 (2022) 121357.
19. G. Yang, Y. Jiao, H. Yan, Y. Xie, C. Tian, A. Wu, Y. Wang, H. Fu, Unraveling the mechanism for paired electrocatalysis of organics with water as a feedstock, *Nat Commun.* 13 (2022) 3125.
20. G. Yang, Y. Jiao, H. Yan, Y. Xie, A. Wu, X. Dong, D. Guo, C. Tian, H. Fu, Interfacial engineering of MoO₂-FeP heterojunction for highly efficient hydrogen evolution coupled with biomass electrooxidation, *Adv Mater.* 32 (2020) 2000455.
21. K. Gu, D. Wang, C. Xie, T. Wang, G. Huang, Y. Liu, Y. Zou, L. Tao, S. Wang, Defect-Rich High-Entropy Oxide Nanosheets for Efficient 5-Hydroxymethylfurfural Electrooxidation, *Angew. Chem., Int. Ed.* 60 (2021) 20253.